Effect of the temperature on the impedance control of pressure-based, current-driven electroacoustic absorbers: Addressing the loss of passivity using a viscoelastic material model

Leonardo Ferreira[1a], Rafael de O. Teloli[a], Emanuele de Bono[b], Morvan Ouisse[a]

[a] *Université Marie et Louis Pasteur, SUPMICROTECH, CNRS, institut FEMTO-ST, F-25000 Besançon, France*
[b] *Ecole Centrale de Lyon, CNRS, ENTPE, LTDS, UMR5513, Lyon, 69130, France*

Abstract

In active noise control, pressure-based control strategies for electroacoustic absorbers depend on the loudspeakers' electromechanical properties, known as Thiele-Small parameters, to implement impedance control. Due to the viscoelastic nature of loudspeaker materials, these parameters are sensitive to environmental conditions, particularly temperature. This study investigates the impact of temperature on the impedance control of electroacoustic absorbers. The acoustic impedance of several absorbers is measured over a broad temperature range, and an analytical model is used to identify the variation of the Thiele-Small parameters with temperature. A viscoelastic material characterization framework is then proposed, employing the Fractional Zener, Generalized Maxwell, and Generalized Fractional Maxwell models. These models are identified for individual absorbers and compared in terms of accuracy and computational cost. A generalized approach through a normalized curve derived from multiple absorbers is introduced to estimate the parameters of unknown absorbers. The pressure-based control law is subsequently updated to include temperature-dependent parameters, enabling evaluation of their influence on absorber passivity. Results demonstrate that adapting the control strategy using either direct measurements or model-based estimations enhances the acoustic passivity of electroacoustic absorbers.

Keywords: Active noise control, Environmental effects, Fractional Zener model, Generalized Fractional Maxwell model, Generalized Maxwell model, Impedance control, Loudspeakers, Viscoelastic materials

1. INTRODUCTION

Noise management is a challenge in various engineering fields, from ambient noise control to mitigating sound in open ducts. Key applications include reducing noise in heating, ventilation, and air conditioning (HVAC) systems, as well as controlling noise in aircraft engines. In these cases, passive noise control techniques are commonly employed, utilizing absorbent materials and honeycomb perforated liners [1]. These liners work based on the quarter-wavelength resonance, and demand larger thickness for efficiency at lower frequencies. An alternative to passive liners is active impedance-based control [2]. These systems can

[1] Corresponding author: leonardo.ferreira@femto-st.fr

outperform conventional acoustic treatments and adapt themselves to the operational regime. Based on this concept, Rivet et al. [3] proposed a broadband set of electroacoustic absorbers (EAs) utilizing a feed forward control architecture. They are composed of a loudspeaker from which a target impedance is achieved on the loudspeaker (the actuator) based on collocated pressure measurements. Several studies have since been conducted to evaluate the efficiency of these devices [1, 4, 5], as well as their limitations. To date, the effects of loudspeaker model uncertainties upon the EA performances, has been investigated by de Bono et al. [6] and Volery et al. [7], but such uncertainties have never been correlated with one of their most impacting causes, which is temperature variation. The most recent application in a scaled test-rig of a turbofan engine [8], where temperatures reach extreme values, demands to deeply investigate this fundamental correlation, in order to realistically envisage a further step forward in the technology readiness level (TRL) of EAs.

The temperature dependency of these devices arises at the material level of the loudspeaker, which may be composed of various materials. The spider, a flexible component that centers the voice coil and provides restoring force during diaphragm motion, typically consists of impregnated textiles such as cotton, poly-cotton, or Nomex, while the surround may include materials like rubber, foam, coated fabrics, or diaphragm materials [9]. These materials exhibit viscoelastic properties [10], and environmental conditions can influence their mechanical characteristics, potentially impacting loudspeaker vibration behavior.

Several studies have proposed methods to evaluate the operating temperature of loudspeakers. Henricksen [11] analyzed the role of heat-transfer mechanisms on voice-coils, deriving a phenomenological relation combining voice-coil temperature, electric input and loudspeaker parameters. Chapman [12] developed a system for real-time simulation of voice-coil and magnet assembly temperatures in moving coil loudspeakers using multiple material systems. Addressing the viscoelastic frequency-temperature dependency, Rousseau and Vanderkooy [13] reported the properties of two loudspeakers with different loss characteristics in temperatures from 20 to 50 °C, while Maillou et al. [14] modeled the nonlinear frequency behavior of a loudspeaker using polynomial nonlinearity and a generalized Hammerstein model.

The dynamics of a loudspeaker is usually modeled in terms of the Thiele-Small parameters [15, 16], characterizing the electromechanical behavior of these devices. These parameters describe how a loudspeaker interacts with both electrical signals and mechanical loads, allowing for the evaluation of performance aspects like frequency response, efficiency and sound quality. Although previous studies have examined the temperature dependence of loudspeaker material properties, a structured approach for identifying viscoelastic behavior across different models remains unaddressed. Furthermore, no prior work in the literature has investigated the passivity issues arising from the impact of temperature on the Thiele-Small parameters of EAs.

To fill this gap, this work evaluates the effect of temperature on the impedance control of EAs by studying the temperature-frequency dependence of the Thiele-Small mechanical parameters of loudspeakers, specifically mass, resistance, and stiffness. The influence of temperature is experimentally analyzed over a range of -10°C to +50°C, and the Thiele-Small parameters are identified. Three viscoelastic models are then employed to characterize the observed behavior: the fractional Zener model, the generalized Maxwell model (GMM), and the generalized fractional Maxwell model (GFMM). The temperature-frequency dependence of the loudspeaker's mechanical properties is assessed by calibrating these viscoelastic models to a master curve generated using the Williams-Landel-Ferry law. Additionally, a normalized viscoelastic model is proposed to generalize information obtained from tested EAs to untested ones. Finally, the passivity of these devices is evaluated under scenarios with and without parameter correction as a function of temperature. Parameter correction is performed using both experimentally observed data and the developed normalized viscoelastic model.

The paper is organized as follows. Section 2 presents the theoretical background, including the mechanical modeling of the loudspeaker, the pressure-based control law applied to the EAs, the Thiele-Small parameter identification procedure, and the fitting of the proposed viscoelastic models. Section 3 describes the experimental setup and the loudspeakers used in this study. Section 4 presents the results of the parameter identification, followed by the viscoelastic model fitting in Section 5. Section 6 provides the passivity analysis of the EAs using temperature-dependent parameters in the control law. Finally, Section 7 summarizes the conclusions and outlines directions for future research.

2. PROBLEM FRAMEWORK AND THEORETICAL BACKGROUND

This work proposes the evaluation of the temperature effects on the impedance control of EAs. For this, the framework presented in Fig. 1 is proposed, based on five steps:

1. To conduct experimental tests on the EAs under varying temperatures to evaluate acoustic impedance according to ASTM E1050-24 [17], within the range of +50°C to −10°C.
2. To identify the Thiele–Small parameters from the mechanical impedance using the polyreference least-squares complex frequency-domain method (PolyMAX).
3. To identify the fractional Zener, generalized Maxwell, and fractional generalized Maxwell models for the mechanical properties, based on master curves derived from the Williams–Landel–Ferry law.
4. To develop a normalized GMM representing the average mechanical properties of three EAs, and evaluate its performance in predicting the parameters of an unknown absorber.
5. To assess the passivity of the EAs under temperature variations and propose a control strategy based on the adaptation of mechanical properties using the normalized viscoelastic model.

The underlying theoretical foundations behind the proposed framework are discussed in the subsequent subsections.

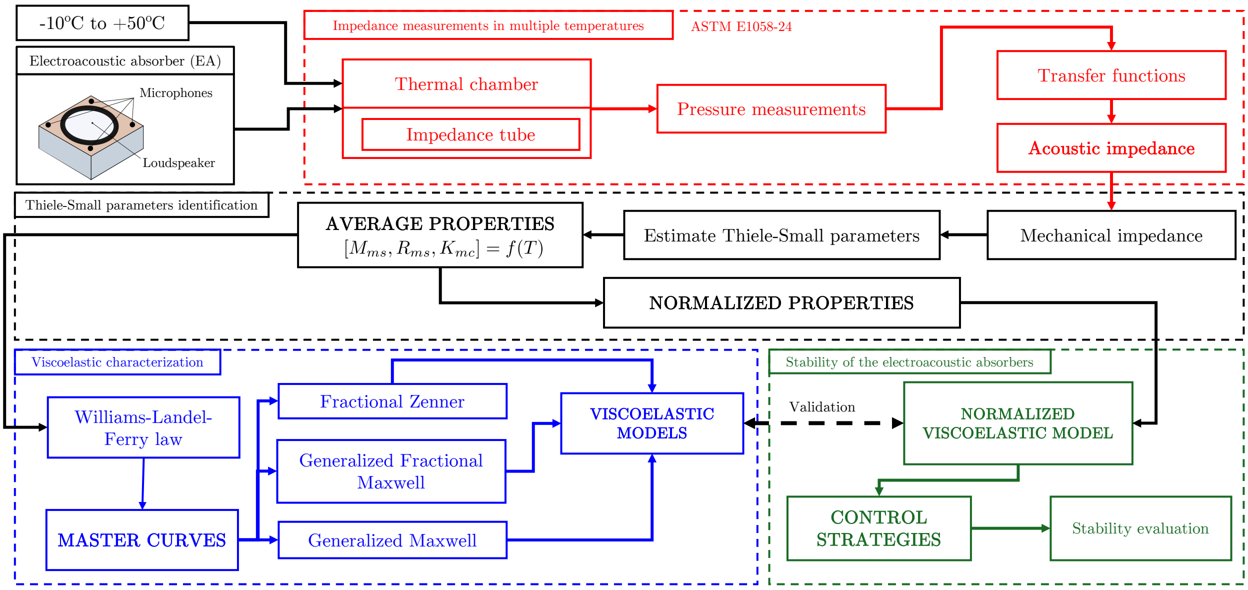

Figure 1: Proposed framework for evaluating temperature effects on the EAs.

2.1. Single-degree-of-freedom loudspeaker model

The electromechanical loudspeaker can be modeled as single-degree-of-freedom (1DOF) oscillator that is driven by a coil with a permanent magnetic field [18]. Figure 2a presents an EA built using a loudspeaker, whereas Fig. 2b showcases the pressure-current control strategy, and Fig. 2c presents a schematic representation of the equivalent free-body diagram of the system. For modeling the mechanical dynamics of the system according to the Newton's second laws, the following hypothesis are considered: (i) forces imposed by the pressure wavefield are small; (ii) the system operates with low displacement in the low-frequency region, being assumed as a linear system. Therefore, the equilibrium of forces yields

$$M_{ms}\frac{dv(t)}{dt} = S_d p(t) - Bli(t) - R_{ms}v(t) - K_{mc}\int v(t)dt, \tag{1}$$

where $v = du/dt$ is the diaphragm velocity, p is the surface pressure at the diaphragm, i is the electrical current flowing through the voice-coil, M_{ms} represents the mass of the driver diaphragm and coil assembly, R_{ms} is the mechanical viscous resistance, S_d is the equivalent area of the driven diaphragm, and Bl is the force factor of the moving coil. K_{mc} is the total mechanical stiffness of the assembled EA, represented as $K_{mc} = 1/C_{ms} + \rho c^2 S_d^2/V_b$, in which C_{ms} is the mechanical compliance of the surrounding suspension and the spider, ρ is the air mass density, c is the speed of sound, V_b is the loudspeaker rear cabinet volume. These mechanical and electrical properties that define the frequency performance of the loudspeaker, i.e., M_{ms}, R_{ms}, K_{mc}, S_d, and Bl, are known as Thielle-Small parameters.

Considering the Laplace variable s and applying the Laplace transform to Eq. (1)

$$S_d P(s) = Z_m(s)V(s) + BlI(s), \tag{2}$$

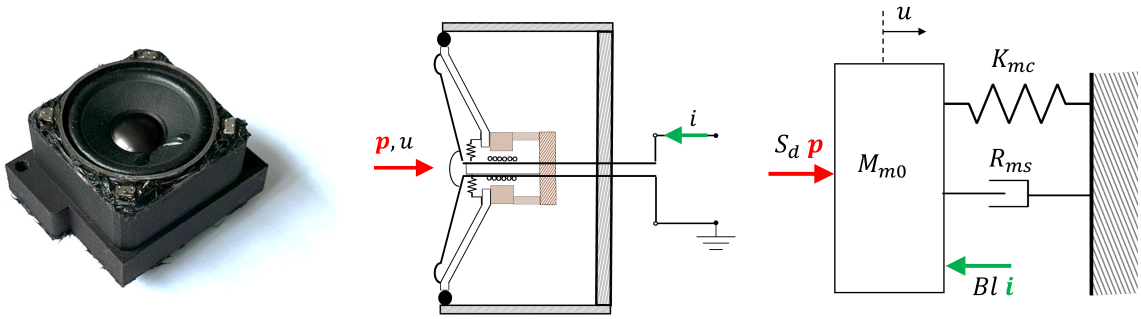

(a) (b) (c)

Figure 2: Loudspeaker considered in this study: (a) EA built with it and (b) free-body diagram.

where Z_m represents the mechanical impedance of the closed-box loudspeaker

$$Z_m(s) = M_{ms}s + R_{ms} + \frac{K_{mc}}{s}. \tag{3}$$

The dynamic response of the diaphragm to an external acoustic disturbance can be described by its acoustic impedance, which is defined as the complex ratio of the total sound pressure $P(s)$ at the diaphragm to the diaphragm velocity $V(s)$. In the condition of open-circuit loudspeaker, i.e., the case where no current circulates through the coil, Eq. (2) yields

$$Z_a(s) = \frac{P(s)}{V(s)} = \frac{Z_m(s)}{S_d}, \tag{4}$$

where Z_a represents the acoustical impedance of the loudspeaker.

The behavior of EAs can be controlled by adjusting their acoustic impedance to a target value. Pressure-based control strategies are proposed by Rivet et al. [3], Guo et al. [19], and de Bono et al. [20]. These control strategies rely on the values for the Thiele-Small parameters to synthesize the control based upon the 1DOF model described by $Z_m(s)$. Given that these parameters are related to the material properties, which are in turn susceptible to environmental influences, there is a need for investigating the variation of the Thiele-Small parameters due to environmental causes.

2.2. Control strategies for pressure-based electroacoustic absorbers

The EAs can be operated to achieve a target acoustic impedance using a pressure-based control law. An extensive discussion on acoustic impedance control using pressure-based approaches is presented by Rivet et al. [3].

Considering a local control strategy [21], the transfer function between the pressure measurements and the imposed current to the loudspeaker coil to implement a target acoustic impedance Z_{at} can be obtained from Eqs. (2) and (4):

$$H(s) = \frac{I(s)}{P(s)} = \frac{1}{B\ell}\left(S_d - \frac{Z_m(s)}{Z_{at}(s)}\right), \tag{5}$$

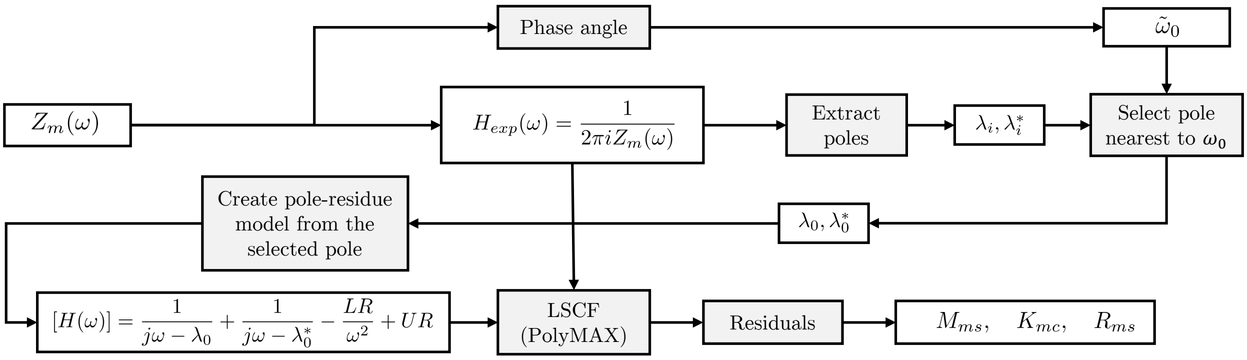

Figure 3: Thiele–Small parameters identification procedure. LSCF stands for Least-Squares Complex Frequency-domain.

where $H(s)$ is the control transfer function and Z_{at} is the target impedance obtained as

$$Z_{at}(s) = \frac{P(s)}{V(s)} = \mu_1 \frac{M_{ms}}{S_d} s + R_{at}\rho_0 c_0 + \mu_2 \frac{K_{mc}}{sS_d}, \tag{6}$$

where μ_1 and μ_2 are two tunable coefficients that allow for controlling the mass and stiffness of the loudspeaker, respectively; R_{at} controls the target impedance to be achieved by the loudspeaker at the resonance, usually expressed as a fraction of the characteristic impedance of the air; ρ_0 is the air mass density, whereas c_0 is the speed of sound.

2.3. Thiele-Small parameters identification

Figure 3 illustrates the Thiele-Small parameter identification procedure based on the measured mechanical impedance. The mechanical impedance is used to derive the experimental frequency response function $H_{exp}(\omega)$. The estimation of the resonance frequency of the absorber ($\tilde{\omega}_0$) is determined from the phase angle of the mechanical impedance, specifically at the frequency where the impedance's imaginary part close to zero. Next, the nearest pole to $\tilde{\omega}_0$ in $H_{exp}(\omega)$ is used to build a pole-residue model $H(\omega)$. Then, the polyreference least-squares complex frequency-domain method (PolyMAX) [22] is used to fit $H(\omega)$ to $H_{exp}(\omega)$ and the model parameters, M_{ms}, R_{ms}, and K_{mc}, are obtained from the residuals.

2.4. Viscoelastic models

Due to the nature of the materials used to build loudspeakers and its surroundings, such as elastomers or treated fabrics, these devices present frequency dependent properties [13]. This frequency dependency can be expressed using the complex Young's modulus representation (E^*)

$$E^*(\omega) = E'(\omega) + jE''(\omega) = E'(\omega)[1 + j\eta(\omega)], \tag{7}$$

where E' is the storage modulus, E'' the loss modulus, $\eta = \tan(\delta) = E''/E'$ is the loss factor, ω is the frequency, and $j = \sqrt{-1}$. Given its complex nature, the frequency dependency is usually represented using modulus/phase, real/imaginary, or real/loss factor (η) plots versus the logarithm of the frequency. In the case of a loudspeaker built using a viscoelastic material, its Thiele-Small stiffness and damping are proportional to the complex modulus, thus they can be represented without loss of generality as

$$K^*(\omega) = K'(\omega) + jK''(\omega) = K'(\omega)[1 + j\eta(\omega)], \tag{8}$$

where K^* is the complex stiffness, K' is the stiffness correspondent to the storage modulus, and K'' is the stiffness correspondent to the loss modulus.

Numerous rheologic representations are available in the literature to model viscoelastic behavior, including representations using spring-dashpot elements [23]. Figure 4 presents the rheologic representation of four common models: the standard linear (Classical Zener), the fractional Zener, the generalized Maxwell, and the generalized fractional Maxwell. To fit these models to the loudspeaker materials, experimental measurements of Thiele–Small parameters over a range of frequencies and temperatures are first performed to characterize the complex stiffness of the system. Applying the time–temperature superposition principle, the data are shifted to form master curves using shift factors determined through the Williams–Landel–Ferry (WLF) law. Subsequently, the viscoelastic models are identified by fitting their parameters to achieve close agreement with the constructed master curves.

2.4.1. Williams-Landel-Ferry law

The Williams-Landel-Ferry (WLF) law is an empirical equation used to describe how the viscoelastic properties of polymers change with temperature near a reference point [24]. It describes how the time-temperature superposition principle can be employed to shift viscoelastic response data, forming a master curve that facilitates the prediction of material behavior across a broad range of timescales. The temperature evolution of the shift factor a_t can be expressed as law

$$\log(a_t) = \frac{-C_1^0(T - T_0)}{-C_2^0 + (T - T_0)}, \tag{9}$$

where T is the temperature under analysis, T_0 is a reference temperature, and C_1^0 and C_2^0 are constants. Then, the reduced frequencies can be expressed as a function of the shift factors

$$f_{at} = f_0 a_t, \tag{10}$$

where f_0 is the natural frequency of the EAs at each temperature.

2.4.2. Fractional Zener model

The classical Zener model, also known as the standard linear solid model, consists of a spring (elastic element) in parallel with a Maxwell element (a spring and dashpot in series) [25]. This configuration can represent the viscoelastic behavior of materials under small deformations by balancing elasticity and

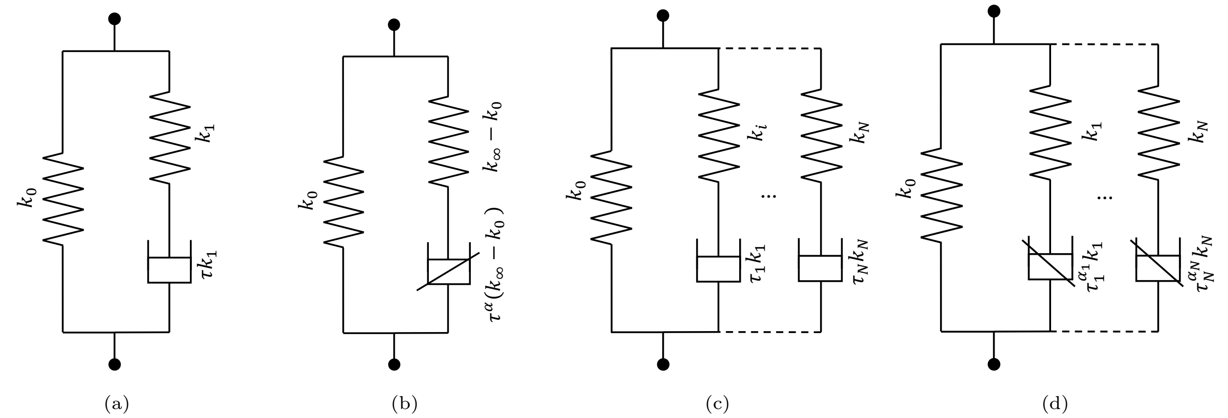

Figure 4: Rheologic representation of viscoelastic models: (a) standard linear (Classical Zener), (b) Fractional Zener, (c) Generalized Maxwell, and (d) Generalized Fractional Maxwell. In the figures, k_i denotes the stiffness of the i-th element, τ_i the relaxation time, and α_i the derivative order of the fractional elements.

viscosity. However, it is limited in its capacity to describe complex real-world responses, particularly over a broad frequency range.

The Fractional Zener expands the classical Zener by including a fractional derivative in the dashpot element. The fractional derivatives allow describing behaviors between purely elastic and purely viscous [26]. The complex stiffness of a viscoelastic material using the fractional Zener model (K^*_{FZ}) with respect to the angular frequency ω can be expressed as

$$K^*_{FZ}(\omega) = \frac{k_0 + k_\infty (j\omega\tau)^\alpha}{1 + (j\omega\tau)^\alpha}, \tag{11}$$

where $k_0 = \lim_{\omega\to 0} K^*_{FZ}(\omega)$, $k_\infty = \lim_{\omega\to\infty} K^*_{FZ}(\omega)$, τ is the characteristic time constant of the system (or relaxation time), and α is the fractional derivative order. The characteristic time constant is defined as

$$\tau = \frac{1}{\omega_{\text{pic}}} \left(\frac{K_0}{K_\infty}\right)^{\frac{1}{2\alpha}}, \tag{12}$$

where ω_{pic} is the angular frequency of maximum damping. The fractional derivative order α is defined as

$$\alpha = \frac{2}{\pi} \arcsin \left[\eta_{\text{pic}}(K_\infty - K_0) \times \frac{2\sqrt{K_0 E_\infty} + (K_\infty + K_0)\sqrt{1+\eta^2_{\text{pic}}}}{\eta^2_{\text{pic}}(K_\infty + K_0)^2 + (K_\infty - K_0)^2} \right], \tag{13}$$

where η_{pic} is the maximum damping rate, at ω_{pic} [27].

2.4.3. Generalized Maxwell model

A GMM is composed of Maxwell cells connected in parallel and the model order is defined by the number of cells [28]. The rheological formulation of this model is given by

$$K^*_{GMM}(\omega) = k_0 + \sum_{i=1}^{N} k_i \frac{j\omega\tau_i}{1 + j\omega\tau_i}, \tag{14}$$

where K^*_{GMM} is the complex stiffness, k_0 is the static stiffness taken at $\omega = 0$, k_i is the stiffness of the i-th spring, and τ_i is the relaxation time of the dashpot. By increasing the number of cells, a GMM model can represent increasingly complex viscoelastic behaviors.

2.4.4. Generalized Fractional Maxwell model

A GFMM is composed of a spring in parallel with multiple fractional Maxwell elements, i.e., multiple fractional springpot elements [28]. The main difference between the GMM and the GFMM is the addition of fractional derivatives to each Maxell cell, thus the model yields

$$K^*_{GFMM}(\omega) = k_0 + \sum_{i=1}^{N} k_i \frac{(j\omega\tau_i)^{\alpha_i}}{1 + (j\omega\tau_i)^{\alpha_i}}, \tag{15}$$

where K^*_{GFMM} is the complex stiffness, k_0 is the static stiffness taken at $\omega = 0$, k_i is the stiffness of the spring, τ_i is the relaxation time of the dashpot, and α_i is the fractional derivative of the i-th cell.

3. EXPERIMENTAL SETUP

Three EAs are evaluated experimentally to define the acoustic impedance of the loudspeakers and account for experimental dispersion. These EAs, also referred as cells A, B and C in the following, are identical from a design perspective. The impedance tube used for the experiments is built in aluminum, has a square cross-section of 50 mm and a length of 300 mm. Three PCB Piezotronics 130F21 microphones are positioned at distances of 100 mm, 150 mm, and 200 mm from the excitation source, and referenced as P1, P2 and P3 in the following, respectively.

Data acquisition is performed using the NI cDAQ-9174 system, with NI 9234 module for data acquisition and NI 9263 module for signal generation. A Stage Line STA-102 amplifier is placed between the signal generator and the input speaker to amplify the input signal. The excitation consists of white noise signal in a frequency range between 100 Hz and 3000 Hz and a sound pressure level (SPL) of 100 dB. The frequency limits are defined based on ASTM E1050-24, considering both the microphone spacing and the cutoff frequency of the tube which is approximately 3430 Hz.

Impedance measurements are conducted across a wide range of temperatures to evaluate the temperature dependency of the mechanical properties. A Climats PCH60 thermal chamber is used to control the temperature of the square impedance tube, covering a range from $-10°$C to $+50°$C. This temperature range is selected mainly by the limitation of the experimental setup. According to the PCB 130F21 specifications, these microphones have an operating temperature range of $-10°$C to $50°$C. Additionally, the current generation the acoustic cells is not designed for very high temperatures, as degradation of polymer parts (mainly in the loudspeaker) is likely to occur.

The impedance tube is mounted at the top of the chamber and subjected to a temperature cycle, as detailed in Fig. 5. The cycle begins with an initial pre-heating phase lasting 90 minutes, during which the

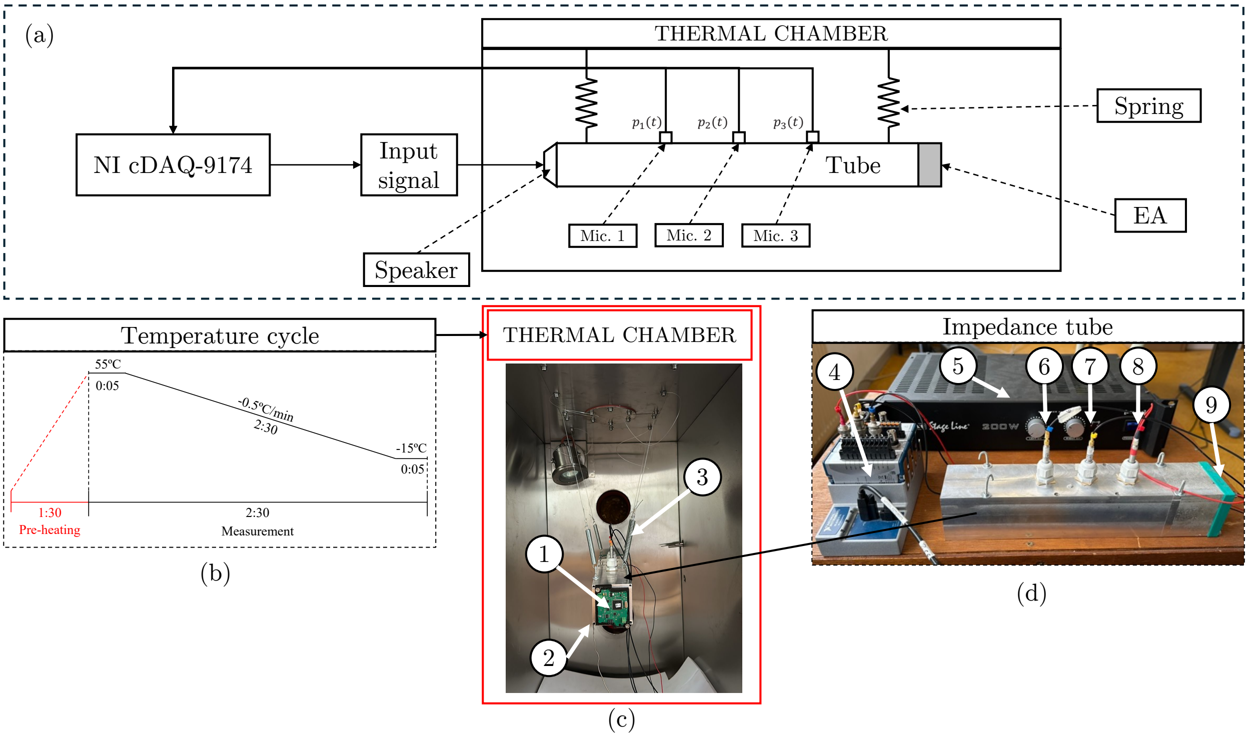

Figure 5: Experimental setup with: (a) schematic description of experiment, (b) temperature cycle, (c) thermal chamber, and (d) impedance tube and electronics. In the figures, the numbers represent (1) the EA, (2) the thermocouple, (3) the springs used to suspend the tube, (4) the NI cDAQ-9174, (5) the Stage Line STA-102 amplifier, and (6) the P1 microphone - PCB 130F21, (7) the P2 microphone - PCB 130F21, (8) the P3 microphone - PCB 130F21, and (9) the PCB input loudspeaker.

temperature is raised to +55°C. Following pre-heating, the temperature is held constant at +55°C for 5 minutes to ensure system stabilization. Then, a constant cooling gradient of -0.5°C/min is applied until the temperature reaches -15°C, followed by a 5-minutes stabilization period. This gradient, together with the high conductivity of aluminum used in the impedance tube construction supports rapid temperature equalization and enforce temperature homogeneity within the tube. The temperature inside the tube is monitored using a thermocouple, and data recorded at temperatures above +50°C and below -10°C are discarded. Three sequential pressure measurements are performed, each during 10 seconds, and the system holds 30 seconds before starting a new round. This cycle is repeated during all the temperature gradient duration, which results in 360 pressure measurements from +50°C to -10°C. Due to the limitations imposed by the automated measurement scheme within the closed environment of the thermal chamber, microphone switching at all temperature, as proposed by the ASTM-1058-24, is not straightforward. Therefore, this procedure was evaluated only at the ambient temperature configuration to compensate for any potential discrepancies between amplitude and phase of the microphones.

The sampling frequency is 51200 Hz and the post-processing is made through a power spectral density computation using the Welch's estimator through a hanning window with 8192 points and a 50% overlapping between adjacent time frames.

Three different EAs similar to the one presented in Fig. 2a and named A, B and C are used in the following. They are identical in their desing, using loudspeakers from the same manufacturer. Differences between them can arise from the manufacturing process of the components, and the assembly of the EA, which is manual.

4. THIELE-SMALL PARAMETERS IDENTIFICATION

The acoustic impedance for the three tested loudspeakers is determined in accordance with ASTM E1050-08. For tests conducted inside the thermal chamber, air density and sound velocity are adjusted for each sample using the formulation proposed in the ASTM E1050-24 [17] and the thermocouple readings.

The effects of the thermal chamber on the impedance measurements were evaluated at several setpoints, where the chamber was briefly switched off (fan and compressor disabled), a measurement was taken, and the result was compared with the measurement acquired during the ramp at the same instantaneous temperature. The on/off results were indistinguishable within the measurement uncertainty, indicating that background noise generated by the chamber equipment does not affect the impedance measurements. This outcome is mainly attributed to the fact that the impedance tube is closed and subjected to an SPL of 100 dB, which is considerably higher than the noise level inside the chamber.

Additionally, two complementary checks were made. (i) At several setpoints, impedance measurements acquired during a continuous temperature ramp were compared, at the same instantaneous temperature, with measurements obtained after the chamber had reached thermal equilibrium; differences were negligible. (ii) Each cell was tested twice on different days to probe variability in external conditions and in the chamber's PID control actions; both runs yielded nearly identical temperature-evolution curves for impedance, confirming repeatability. Collectively, these checks indicate that although the tube is not rigidly anchored to the chamber walls, chamber-induced vibrations did not bias the measured impedance under normal operating conditions.

4.1. Temperature influence on Thiele-Small parameters

Figure 6 illustrates the acoustic impedance near resonance and the corresponding FRFs in displacement per unit force for loudspeakers A, B, and C, evaluated at 5°C increments. The three loudspeakers exhibit similar temperature-dependent behaviors, with the real part of the impedance reaching a minimum value around resonance, and the imaginary part being negative before resonance and positive after it. Notably, the real part of the impedance remains stable with respect to temperature below the characteristic impedance of air (represented by the dashed black line) near resonance. Outside resonance, the impedance increases

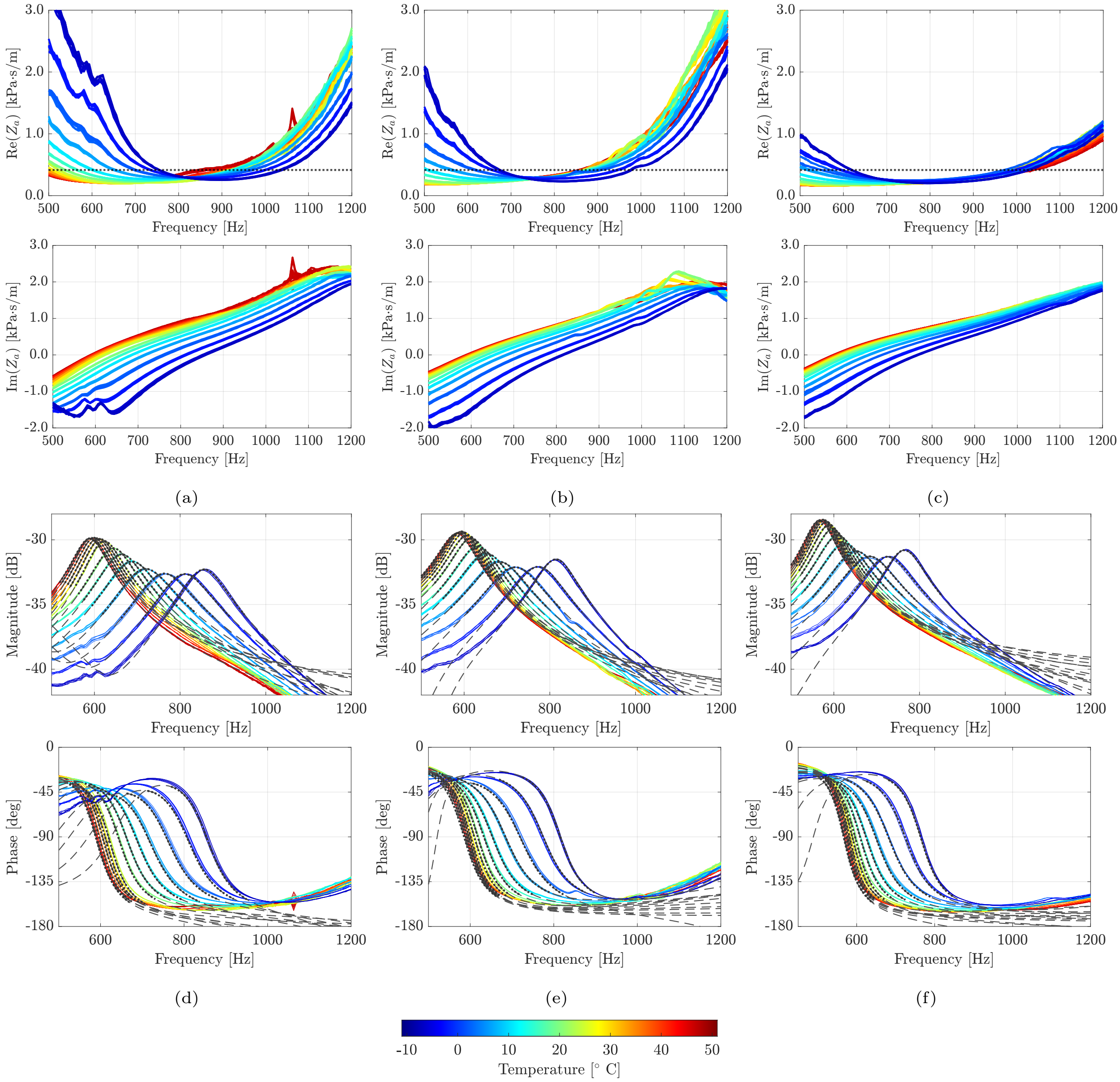

Figure 6: Experimental results obtained from the impedance tube: real (Re) and imaginary (Im) measurements for the acoustic impedance from -10°C to 50°C for (a) cell A, (b) cell B, and (c) cell C. In the impedance curves, the dotted horizontal line represents the typical air impedance at room temperature (415 Pa.s/m); and magnitude and phase of the FRF calculated from the mechanical impedance for (d) cell A, (e) cell B, and (f) cell C. In the FRFs, the dashed lines represents the model obtained using PolyMAX, with the region used for the fitting process (-3.5 dB from resonance) highlighted in with dots.

rapidly, with this behavior becoming more pronounced below 10°C, when it sharply rises. This occurs primarily due to the larger shift in the natural frequency of the loudspeaker at lower temperatures.

Figure 6(d–f) shows the FRFs in displacement per unit force, obtained by converting the acoustic impedance to mechanical impedance using Eq. (4). The PolyMAX model reproduces the system behavior

Table 1: Resonance frequencies for EAs A, B, and C. The variation in resonance frequency is expressed relative to the value at 20°C, which is used as the reference.

	Cell A		Cell B		Cell C	
Temperature [°C]	**Resonance frequency [Hz]**	**Variation [%]**	**Resonance frequency [Hz]**	**Variation [%]**	**Resonance frequency [Hz]**	**Variation [%]**
-10	856.2	32.2	818.8	31.4	766.7	27.3
0	762.5	17.7	722.9	16.1	685.4	13.8
10	689.6	6.4	658.3	5.7	629.2	4.5
20	647.9	-	622.9	-	602.1	-
30	616.7	-4.8	608.3	-2.3	589.6	-2.1
40	602.1	-7.1	597.9	-4.0	579.2	-3.8
50	591.7	-8.7	591.7	-5.0	572.9	-4.8

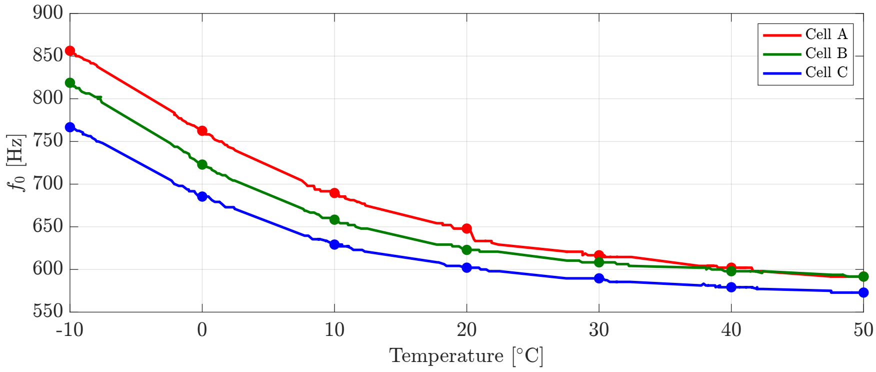

Figure 7: Natural frequency for three loudspeakers measured from -10 to 50°C.

in the vicinity of the primary resonance in both magnitude and phase. Because the identification employs a 1-DOF model, fidelity degrades away from resonance. The choice of a 1-DOF model is motivated by the need for a low-order representation to implement real-time control on the embedded microcontroller and to mitigate instabilities [6], as well as by the fact that the loudspeaker acts as an absorber predominantly around its resonance, where a single, clearly identifiable mode dominates, as evidenced by the impedance curves and FRFs.

Table 1 and Fig. 7 present the resonance frequency for the loudspeakers of the EAs A, B, and C. The resonance frequency can be tracked by identifying the points where the imaginary part of the impedance are closer to zero. At 20°C, the loudspeakers A, B, and C present natural frequencies of 647.9 Hz, 622.9 Hz, and 602.1 Hz, respectively. Between 20°C and 50°C, the natural frequency of the system varies to 591.7 Hz for loudspeaker A, 591.7 Hz for loudspeaker B, and 572.9 for loudspeaker C, which represents variations of -8.7%, -5.0%, and 4.8% variation, respectively. In the range from 20°C to -10°C, the natural frequency shifts to 856.2 Hz, 818.8 Hz, and 766.7 Hz for loudspeakers A, B, and C, representing variations of 32.2%, 31.4% and 27.3%, respectively. This behavior indicates non-linear changes in the material properties as a function of temperature. This phenomena can also be observed by the fact that, between 50°C and 20°C, the curves are closely grouped, but they diverge significantly below 20°C.

The method outlined in Section 2.3 is applied to identify the Thiele-Small parameters of the EAs. Figure 6d-f presents the FRFs obtained using mechanical impedance. For the identification process, the assumption of a 1DOF system is valid only near resonance, therefore boundaries are applied with a -3.5 dB criterion. The change in natural frequency is even more apparent while evaluating the FRFs.

Figure 8 and Tab. 2 present the estimated Thiele-Small parameters with respect to temperature for the loudspeakers A, B and C. Note that the mass of the three loudspeakers remains almost constant, with small experimental variations likely due to measurement noise. In contrast, the resistance and stiffness exhibit nonlinear behavior. Resistance increases from -10°C and reaches a maximum near 0°C, after which it decreases and stabilizes around 30°C. The stiffness decreases with temperature with a greater rate of change below 20°C, then reduces its rate of decreasing. This non-linearity in stiffness corresponds to the behavior observed in the resonance frequency above and below 20°C.

Table 2: Mechanical Thiele-Small parameters identified for temperature range from -10°C to 50°C for loudspeakers A, B, and C. For this study, the values measured at 20 °C are considered as reference.

Loudspeaker	**Parameter**	**Temperature [°C]**							**Mean**	**STD.**	**CV [%]**
		-10	**0**	**10**	**20**	**30**	**40**	**50**			
A	M_{ms} [g]	0.525	0.545	0.542	0.551	0.586	0.589	0.592	0.562	0.027	4.8
	R_{ms} [Ns/m]	0.324	0.402	0.355	0.298	0.266	0.266	0.274	0.312	0.052	16.5
	K_{mc} [kN/m]	15.2	12.6	10.1	9.1	8.7	8.4	8.2	10.3	2.64	25.6
B	M_{ms} [g]	0.508	0.488	0.502	0.507	0.504	0.498	0.498	0.501	0.007	1.3
	R_{ms} [Ns/m]	0.287	0.370	0.323	0.259	0.240	0.239	0.251	0.281	0.049	17.5
	K_{mc} [kN/m]	13.3	10.1	8.5	7.6	7.2	6.9	6.7	8.6	2.36	27.4
C	M_{ms} [g]	0.470	0.459	0.474	0.480	0.493	0.498	0.498	0.482	0.015	3.1
	R_{ms} [Ns/m]	0.255	0.324	0.278	0.225	0.203	0.198	0.203	0.241	0.047	19.7
	K_{mc} [kN/m]	10.9	8.5	7.3	6.8	6.6	6.5	6.3	7.6	1.65	21.8

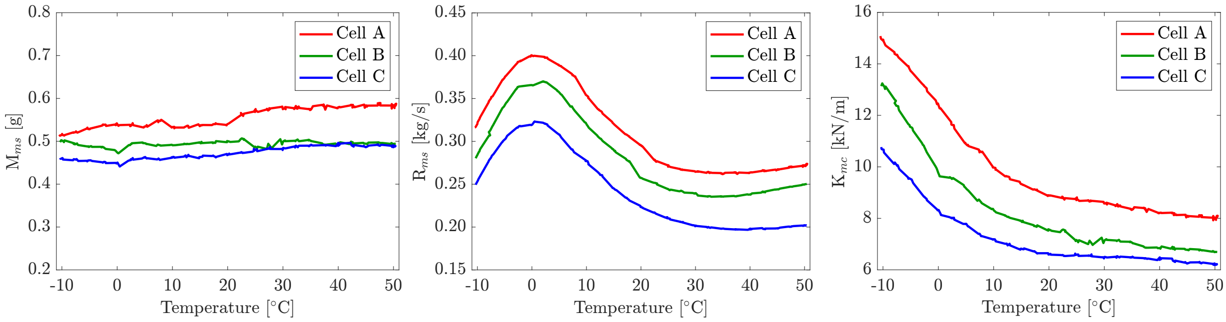

(a) (b) (c)

Figure 8: Thiele-Small parameters with respect to temperature. Estimated properties: (a) M_{ms}, (b) R_{ms}, and (c) K_{mc} for three loudspeakers.

5. VISCOELASTIC MODEL

Due to the comparable behavior of properties across different EAs, a general approach to describe the material is proposed. To achieve this, three viscoelastic models are investigated: the fractional Zener model, the GMM, and the GFMM.

5.1. Master curve

A viscoelastic model requires the complex modulus properties to be represented as functions of frequency and temperature. Since the loudspeaker properties are determined using FRFs, the resonance frequencies at each temperature are considered as the vibration frequency of the loudspeaker at that specific temperature. Using the resonance frequency and temperature data, curves for the storage modulus and loss factor are constructed. The WLF law is applied to calculate the shift factors for each frequency-temperature pair, as illustrated in Fig. 9a, allowing for the construction of a master curve, based on reduced frequency (f_{at}). These shift factors enable the development of a reduced frequency curve containing the storage modulus and loss factor plots, as shown in Figs. 9b and 9c. The following subsections present the fitting of the properties for cell A.

5.2. Model fitting

5.2.1. Fractional Zener

The fractional Zener model involves four parameters for fitting: k_0, k_∞, ω_{pic}, and η_{pic}. The frequency and maximum loss factor can be directly evaluated from Fig. 9c, yielding values of 5250 Hz and 0.156, respectively. Using these parameters, k_0 and k_∞ are determined through constrained nonlinear optimization, with bounds established based on the projected asymptotes in Fig. 9b, i.e., 1 kN/m and 30 kN/m. The fractional Zener model is adjusted for two different scenarios: (i) for a general fitting for the complete

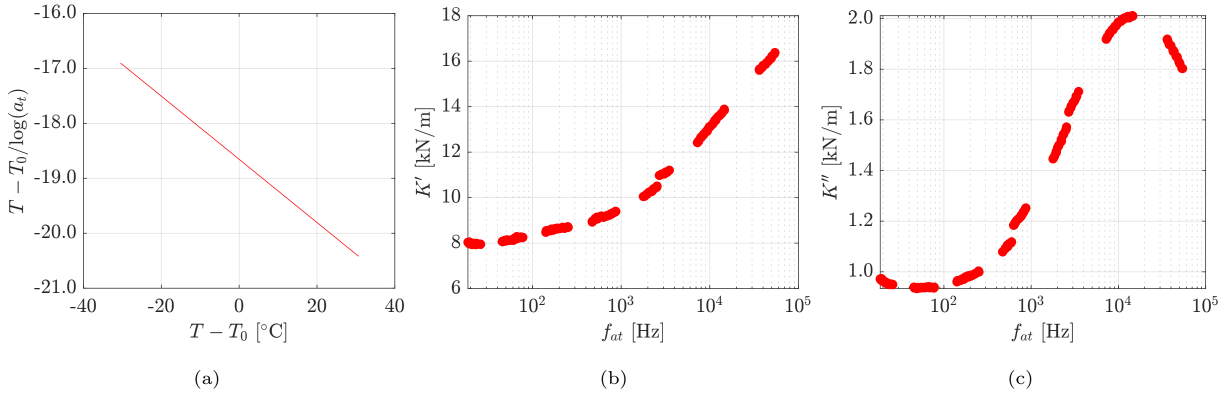

Figure 9: Master curve for cell A obtained using the Wiliam-Landel-Ferry law: (a) translation factors, (b) real part of the stiffness, and (c) imaginary part of the stiffness for cell A.

frequency spectra and (ii) for a reduced fitting considering only frequencies above 4×10^2 Hz. This limit is selected because it represents the first inflection point in the imaginary component of K''. Figure 10 display the optimized Zener model for the complete and reduced frequency spectra.

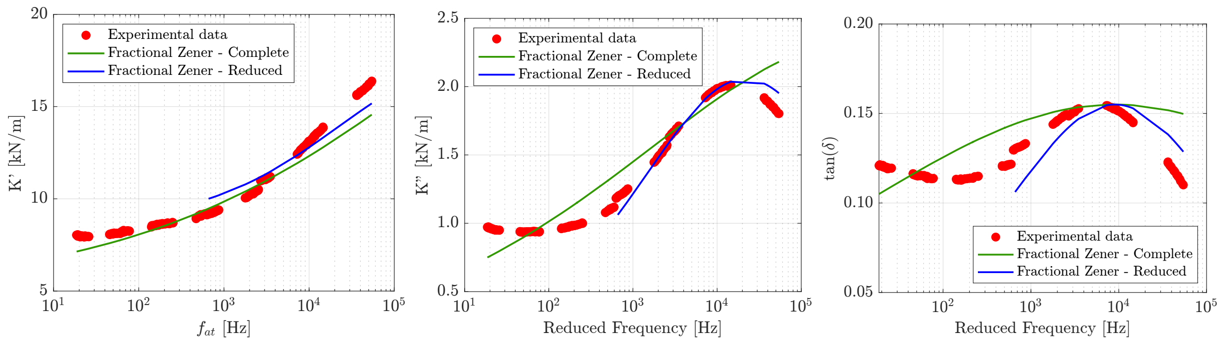

Figure 10: Real and imaginary components of the stiffness and loss factor of the optimized Fractional Zener models for cell A. "Complete" refers to the model identified using the entire frequency spectrum, while "Reduced" refers to the model considering f_{at} above 4×10^2 Hz.

While the fractional Zener model effectively fits most of the storage modulus, it demonstrates limitations in accurately capturing the loss factor, particularly in the low and high reduced frequency regions. When fitting the complete frequency spectra, the model cannot achieve satisfactory results for the imaginary part, even though it respects the maximum value of $\tan(\delta)$ which is equal to 0.156. This indicates that the model lacks the capacity of representing a material with double curvature in its damping response. The fractional Zener is able to describe a behavior with single glass transition with $\lim_{\omega \to 0} \mathrm{Im}(K^*) = \lim_{\omega \to \infty} \mathrm{Im}(K^*) = 0$ and a monotonic evolution of the loss factor before and after the glass transition. However, the experimental data do not agree with this, as the loss factor increases below 200 Hz, in Fig. 10. The parameters of the fitted models are presented in Tab. 3.

Table 3: Identified parameters for the fractional Zener model considering the complete and reduced data sets.

	k$_0$ [kN/m]	**k$_\infty$ [kN/m]**	α
Complete	6.2	23.7	0.297
Reduced	7.1	22.0	0.343

5.2.2. Generalized Maxwell and fractional Zener models

As the Fractional Zener model is unable to fully describe the behavior of the material, GMMs and GFMMs are proposed. These models can effectively capture a wide range of viscoelastic behaviors but involve a trade-off with the increased complexity of a multivariate identification problem.

From an optimization point of view, the GMM model identification is defined as

$$\min_{k_0,k_i,\tau_i} \mathcal{L}(k_0,k_i,\tau_i) = \frac{1}{MN}\sum_{j=1}^{M}\sum_{i=1}^{N}\left(\left(\frac{K'_{\mathcal{M}}(\omega_j)-K'_E(\omega_j)}{K'_E(\omega_j)}\right)^2+\left(\frac{K''_{\mathcal{M}}(\omega_j)-K''_E(\omega_j)}{K''_E(\omega_j)}\right)^2\right), \tag{16}$$

$$\text{subject to} \quad k_0>0, \quad k_i>0,\, \tau_i>0, \qquad i=1,\dots,N, \tag{17}$$

where $K'_{\mathcal{M}}$ and $K''_{\mathcal{M}}$ are the real and imaginary part of the complex stiffness predicted by the GMM from Eq. (14), K'_E and K''_E are the real and imaginary parts of the experimental complex stiffness, k_0 is the static stiffness of model, k_i is the stiffness of the spring in the i-th cell, τ_i is the time constant of the dashpot in i-th cell, and N is the number of cells, and M is the number of j-th discrete frequencies. Therefore, each optimization problem has $2N+1$ parameters consisting of one value for k_0 and values for k_i and τ_i for each cell in Eq. (14). To account for physical constraints, k_0, k_i, and τ_i must be positive.

For the GFMM model, the addition of the fractional derivative adds a new parameter to the optimization, which is defined as

$$\min_{k_0,k_i,\tau_i,\alpha_i} \mathcal{L}(k_0,k_i,\tau_i,\alpha_i) = \frac{1}{MN}\sum_{j=1}^{M}\sum_{j=1}^{N}\left(\left(\frac{K'_{\mathcal{M}}(\omega_j)-K'_{E,i}(\omega_j)}{K'_E(\omega_j)}\right)^2+\left(\frac{K''_{\mathcal{M}}(\omega_j)-K''_E(\omega_j)}{K''_E(\omega_j)}\right)^2\right), \tag{18}$$

$$\begin{aligned} \text{subject to} \quad & k_i>0,\, \tau_i>0, \qquad && i=1,\dots,N, \\ & 0<\alpha_i<1, && i=1,\dots,N, \end{aligned} \tag{19}$$

where α_i is the fractional order of each cell. Therefore, the optimization problem has $3N+1$ parameters consisting of one value for k_0, and values for k_i, τ_i, and α_i for each cell in Eq. (15). In addition to the constraints on k_i and τ_i, the partial derivative order α_i must be between 0 and 1.

The reduced frequency of the system ranges between 10^1 Hz and 10^5 Hz in Fig. 9b and 9c. To avoid a highly unconstrained problem, additional constraints are imposed to the first and last values of τ to ensure that there are anchor points on the limits of the search domain in the format of

$$10^0 < 1/\tau_1 < 10^1, \text{and}$$

$$10^5 < 1/\tau_N < 10^6.$$

This means that the optimizer must search for at least one anchor point at each border of the domain in the form of τ_1 and τ_N. In preliminary evaluations, this increased considerably the stability of the optimization strategy compared to a scenario without any limitation on the borders of the search region. For the remaining parameters $[\tau_2 : \tau_{N-1}]$ the optimizer is limited between 10^1 and 10^5 Hz.

An optimization process based on particle swarm (PSO) [29] is proposed, as depicted in Fig. 11. The optimization process begins by defining the order of the GMM (or GFMM). Based on this order, the PSO algorithm generates a particle swarm with candidates within the search space, corresponding to values of the parameters k_i and τ_i. For each candidate, the complex stiffness is computed and compared with experimental values using the loss function within the optimization process defined by Eqs. (16) and (18). The optimizer evaluates the convergence of the loss and iteratively generates new particle swarms until the loss converges.

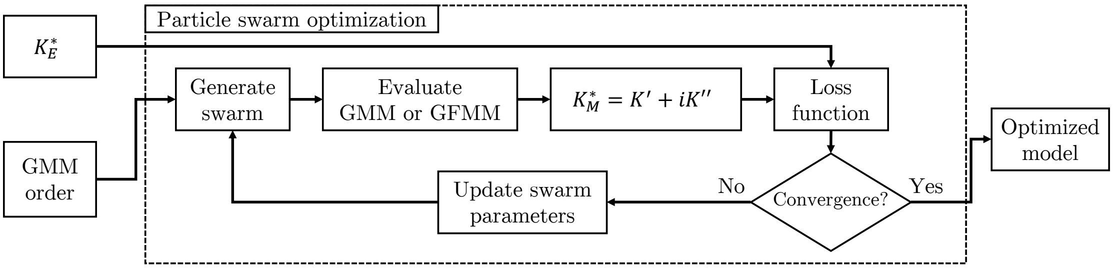

Figure 11: GMM and GFMM optimization process using the particle swarm algorithm.

Figure 12 presents the real and imaginary parts of the fitted GMM, along with the loss factor $\tan(\delta)$ considering multiple model orders. For low-order models, such as third and fourth orders, the results exhibit oscillatory behavior. As the model order increases, the fitted model stabilizes. Conversely, GMMs with orders higher than five can describe both the real and imaginary parts of the material stiffness with increasing accuracy. This contrasts with the results obtained using the fractional Zener model, as shown in Fig. 10, highlighting the superior generalization capability of the GMM model.

Figure 13 shows similar results for the GFMM model. In lower-order models, the real and imaginary parts of the fitted GFMM also exhibit oscillatory behaviors, with the oscillations being more pronounced in the imaginary part of the stiffness. In higher order models, this oscillation reduces progressively.

As the results depend on the order of the GMM and GFMM, Fig. 14 illustrates the convergence analysis of the mean squared error (MSE) and optimization time for the GMM and GFMM as functions of model order. A total of 20 simulations are performed for each model order to account for the variability in the PSO algorithm results. The results demonstrate that the model error decreases with increasing model order, stabilizing at approximately 0.65 for orders 6 and above for the GFMM and at order 7 for the GMM.

For lower-order models, the GFMM exhibits lower dispersion and convergence comparable to the GMM, as shown by the smaller quartile sizes in the box plots for orders 5 and 6. Further analysis up to order 20

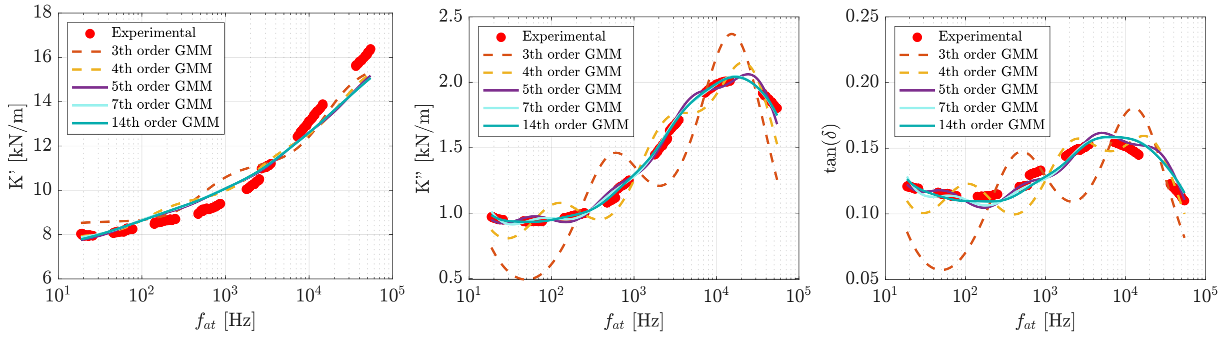

(a) (b) (c)

Figure 12: Results for the process of identification of GMM of order 3, 4 5, 7 and 14: (a) real part of the stiffness, (b) imaginary part of the stiffness. and (c) loss factor.

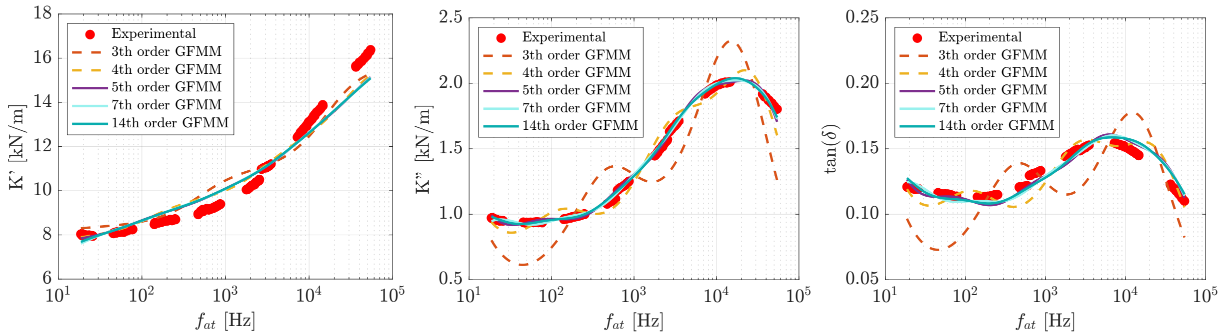

(a) (b) (c)

Figure 13: Results for the process of identification of GFMM of order 3, 4 5, 7 and 14: (a) real part of the stiffness, (b) imaginary part of the stiffness. and (c) loss factor.

confirms this stabilization in the MSE. However, despite its stable average error, the GFMM model exhibits instabilities in the form of outliers for higher orders (e.g., orders 16–20). This behavior is attributed to the model's sensitivity to the values of α_i in each cell; in higher-order models, the optimizer must simultaneously search across multiple cells, increasing the complexity of the optimization process. An optimal balance between accuracy and complexity is observed at approximately order 9. Further simulations with higher-order models did not result in a reduced MSE. Despite multiple optimization strategies and solvers being tested, the MSE could not be reduced below ≈ 0.5 when fitting the real and imaginary parts of the complex stiffness simultaneously. When each component was fitted independently, the model achieved near-zero MSE, indicating that the model structure can reproduce either component in isolation. However, coupling between the real and imaginary parts in the joint objective introduces a trade-off and discrepancies in the real-part stiffness response dominate (Figs. 12a and 13a), producing an apparent error floor around 0.5. Additionally, the non-smooth experimental data, seen as jumps at 600 Hz and 2500 Hz on Fig. 10 could be fitter only with very high order models (with a low physical meaning). These jumps lead to residual values

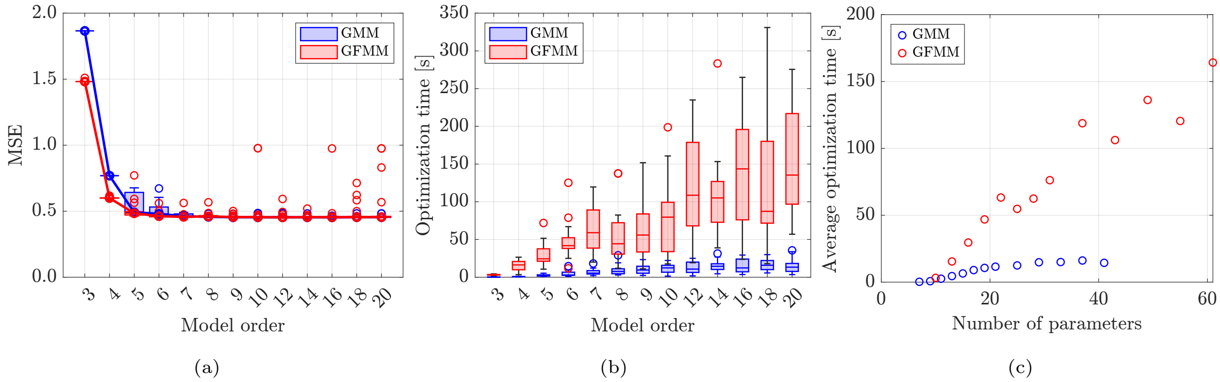

Figure 14: Convergence analysis for the GMM and GFMM optimization process using the PSO: (a) mean square error (MSE) convergence with respect to the model order , (b) average optimization time with respect to the model order, and (c) average optimization time with respect to the number of parameters.

which cannot be lowered with the considered smooth models.

From the computational point of view, the GFMM model is significantly more intensive. Figure 14b illustrates the dispersion of the time required for one optimization round as a function of model order. The computational time for the GFMM model is substantially higher than that for the GMM model. For instance, a sixth-order GMM requires a median computation time of 3 seconds, while the GFMM requires a median of 42 seconds for the same task. At higher orders, the difference becomes even more pronounced. For a 20th-order model, the GMM requires 13 seconds, whereas the GFMM requires 135 seconds.

This increase in computational time can be further analyzed by evaluating the average time required for one optimization round as a function of the number of parameters in the model, as shown in Fig. 14c. The GFMM model is significantly more costly to fit, with an average computation time of 164 seconds for a model with 61 parameters. In comparison, a GMM model of similar size can be optimized in 23 seconds. Furthermore, a GMM model with 201 parameters can be fitted in approximately 50 seconds, whereas a GFMM model of the same size was not trained due to an estimated optimization time of approximately 600 seconds, based on extrapolation from Fig. 14c. The variability introduced by the derivative parameter in the GFMM model increases the complexity of the optimization problem, causing the optimizer to require significantly more time to converge to an optimal solution. Therefore, for both viscoelastic models, an order between 7 and 10 offers the best trade-off considering error reduction and computational cost.

It is important to emphasize that the reported times are related to model optimization, not deployment. For a single forward evaluation of the fitted models, the computational costs are 6.9, 16.0, and 117.8 μs for the Fractional Zener, GMM, and GFMM models, respectively. Given a controller sampling period of 20 μs (50 kHz) for the EAs [6] and the fact that temperature gradients in typical applications are on the order of °C/min, parameter updates can be performed at multi-second intervals outside the high-rate control loop. Consequently, any of the models can be employed in real-time operation.

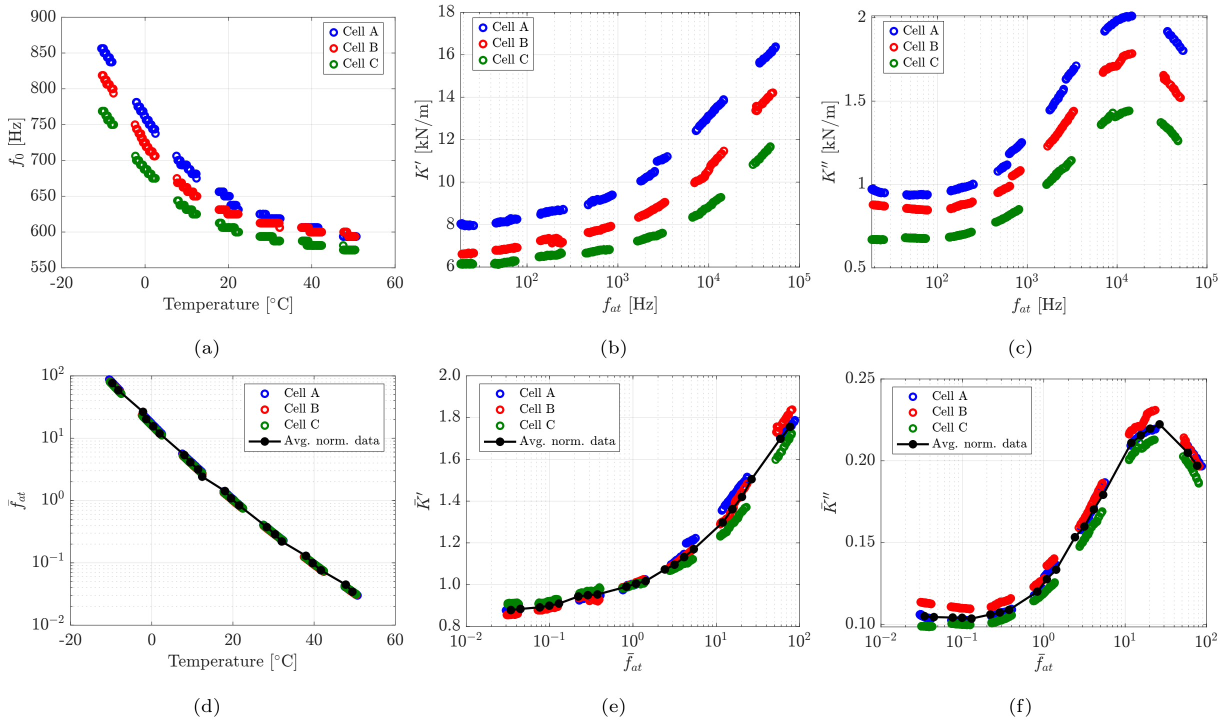

Figure 15: Properties of cells A, B, and C before and after normalization: (a) natural frequency, (b) storage modulus, and (c) loss factor. The properties are normalized using the reference values (K_{ref} and f_{0ref}), yielding: (d) normalized reduced frequency ($\bar{f}_{at}$), (e) normalized storage stiffness ($\bar{K}'$), and (f) normalized loss stiffness ($\bar{K}''$). The normalized plots also include the average of the normalized properties, shown in black. In the figure legends, "Avg. norm. data" refers to the average of the normalized data.

5.3. Normalized viscoelastic model

Given that the EAs are identical from a design perspective, their mechanical properties are expected to exhibit some degree of similarity. Examining the trends in M_{ms}, R_{ms}, and K_{mc} of the EAs in Fig. 8, one can observe a consistent pattern with a visible offset in the average values. This trend persists in f_0 and in K' and η after applying the WFL law, as shown in Fig. 15a-c. This suggests the feasibility of developing a generalized viscoelastic model capable of describing multiple EAs. Such a model would take as input a reference value for an absorber and a target temperature, yielding an estimate of the properties at this temperature.

To build this generalized model, the properties of the EAs A, B, and C are normalized using the Thiele-Small parameters at the temperature of 20°C, as this condition can be imposed in using an air-conditioning system. Subsequently, the normalized storage modulus ($\bar{K}^*$) can be calculated as

$$\bar{K}^* = \frac{K^*}{K_{ref}} = \frac{K'}{K_{ref}}(1 + i\eta), \tag{20}$$

where K_{ref} is the reference stiffness at 20°C. The normalized reduced frequency (f_{at}) obtained from the

WFL law can be defined as

$$\bar{f}_{at} = \frac{f_0}{f_{0_{ref}}} \times 10^{\dfrac{-C_{1_0}(T - T_{ref})}{C_{2_0} + (T - T_{ref})}}, \tag{21}$$

where $f_{0,ref}$ is the reference natural frequency at 20°C. The normalized properties and their averaged values are shown in Figs. 15d to 15f.

A 10th-order GMM is fitted to the averaged normalized data following the optimization process described in Section 5.2.2. Figures 16a, 16c, and 16b illustrates the normalized values of K', K'', and f_0, respectively, as represented by the normalized experimental data and the GMM. To use the GMM for prediction, one can select a target temperature value in Fig. 16a (for instance represented by the sample points in red) and determine the corresponding value of the normalized reduced frequency. Then, by evaluating the GMM model, the real and imaginary part of the normalized stiffness can be obtained. The normalization process can subsequently be reversed using the reference values at 20°C in Eqs. (20) and (21).

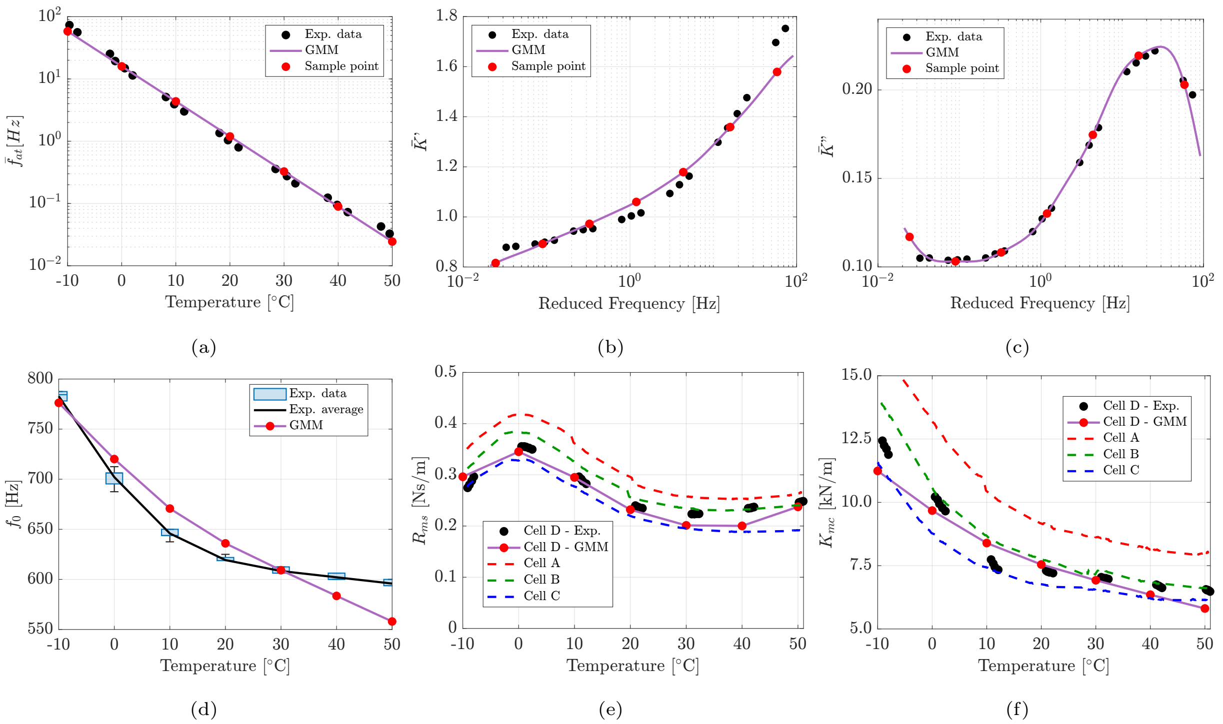

Figure 16: Results for the process of identification of a GMM of order 10 to the normalized data: (a) temperature-reduced frequency relationship. In the charts, red dots depicts selected temperature samples evaluated at -10, 0, 10, 20, 30, 40 and 50 °C to evaluate the model normalized model, (b) normalized real part of the stiffness, and (c) normalized imaginary part of the stiffness. These normalized samples are also used to reconstruct the properties for cell D: (d) f_0, (e) R_{ms}, and (f) K_{mc}.

To assess the performance of the normalized model, a fourth EA, designated as cell D, is introduced. This EA was tested using the same protocol defined in Section 3, but its properties were not included in the development of the viscoelastic model. The GMM is sampled at temperatures of -10, 0, 10, 20, 30, 40, and

50°C (represented by red dots in Figs. 16d–f) and used to estimate R_{ms} and K_{ms}. The estimated values follow the same trend as the experimentally measured ones, although an underestimation is observed at both low and high temperatures. This can be attributed to the viscoelastic model, which underestimates the real part of the stiffness at lower and higher reduced frequencies. Nevertheless, the overall trend of decreasing resonance frequency with increasing temperature is captured by the estimated values. Table 4 compares the natural frequency values for cell D obtained experimentally and those estimated by the normalized GMM. Notably, the error remains below 10% across the entire temperature range. If a fixed value at ambient temperature were used instead, the error in the predicted natural frequency would be –26.4% at –10°C and 3.7% at higher temperatures.

Table 4: Comparison of the results for cell D using the viscoelastic model.

T [°C]	$\mathbf{f0_{exp}}$	$\mathbf{f0_{model}}$	**Difference [%]**
-10	782.8	776.2	0.8
0	702.1	720.1	-2.6
10	645.8	670.7	-3.9
20	619.3	636.0	-2.7
30	608.3	609.2	-0.1
40	602.1	583.5	3.1
50	595.8	558.0	6.4

6. IMPACTS OF THE TEMPERATURE ON THE PASSIVITY OF EAS

After evaluating the temperature effects on the Thiele–Small parameters, characterizing a viscoelastic model for individual EAs, and developing a normalized model to estimate the properties of unknown EAs, the influence of temperature on these devices during operation is assessed. To this end, three strategies are considered:

- **Strategy #1** assumes no prior knowledge of the EA beyond its properties measured at ambient temperature.
- **Strategy #2** adapts the properties of the EA using experimentally measured Thiele-Small parameters.
- **Strategy #3** employs the 10th-order viscoelastic model to approximate the Thiele-Small parameters, allowing adaptation of both the control parameters and system properties as temperature varies.

These three strategies are designed to assess different levels of information availability regarding the EAs in a practical application: (1) a scenario in which only the reference properties at ambient temperature are available; (2) a scenario where a complete set of experimentally measured properties is accessible; and (3) an intermediate case, more representative of practical applications, where reference parameters at 20°C are available and their variation with temperature is estimated using the viscoelastic model.

The influence of temperature on the EAs is evaluated over a broad frequency range by adjusting the control parameters μ_1, μ_2, and R_{at} from Eq. (6). Given that the target mass and target stiffness are defined in terms of the control parameters μ_1 and μ_2 as $M_{at} = \mu_1 M_{ms}$ and $K_{at} = \mu_2 K_{mc}$, respectively, the target frequency of the system can be expressed as

$$f_t = \frac{1}{2\pi}\sqrt{\frac{K_{at}}{M_{at}}} = f_0\sqrt{\frac{\mu_2}{\mu_1}}, \tag{22}$$

where f_t is the target frequency in Hz. The mass control parameter μ_1 is maintained at a constant value of 0.4 due to passivity concerns previously demonstrated by de Bono et al. [6]. Therefore, the target frequency is adjusted by varying μ_2, while R_{at} is modified to control the bandwidth.

For Strategy #1, as the Thiele-Small parameters are considered constant, μ_2 is defined by a discrete set of values: $[0.2, 0.4, 1.0, 2.0]$. Conversely, in Strategies #2 and #3, the Thiele-Small parameters vary with temperature, and the control parameters are adapted accordingly to achieve the same target frequencies defined in Strategy #1. The three strategies are summarized in Table 5, with cells A and D under analysis. For cell A, all properties are assumed to be available. For cell D, only the properties at ambient temperature are considered known, with their temperature dependence estimated using the viscoelastic model.

Table 5: Strategies used to evaluate the influence of the temperature on the performance of the EAs

Strategy	**Description**	**Cell**	**Thiele-Small parameters**	**Control parameters** μ_1	μ_2	$\mathbf{R_{at}}$
#1	Constant Thiele-Small parameters	A	Table 2	0.4	[0.2 0.4 1.0 2.0]	[0.5 1.0 2.0]
#2	Variable Thiele-Small parameters using experimental results	A	Table 2	0.4	[0.1 - 2.5]	[0.5 1.0 2.0]
#3	Variable Thiele-Small parameters from the viscoelastic model	D	Figure 16	0.4	[0.1 - 2.5]	[0.5 1.0 2.0]

The absorption coefficient under normal incidence is used as a performance metric for the EAs. It is defined as

$$\alpha(\omega) = 1 - |R(\omega)|^2, \tag{23}$$

where $\alpha(\omega)$ denotes the absorption coefficient and $R(\omega)$ is the reflection coefficient, given by

$$R(\omega) = \frac{z-1}{z+1}, \tag{24}$$

with the reduced impedance defined as $z = Z(\omega)/\rho c$.

The absorption coefficient quantifies the proportion of incident acoustic energy absorbed by the wall. A value of 1 indicates total absorption, meaning the EA fully absorbs the incident wave with no reflection.

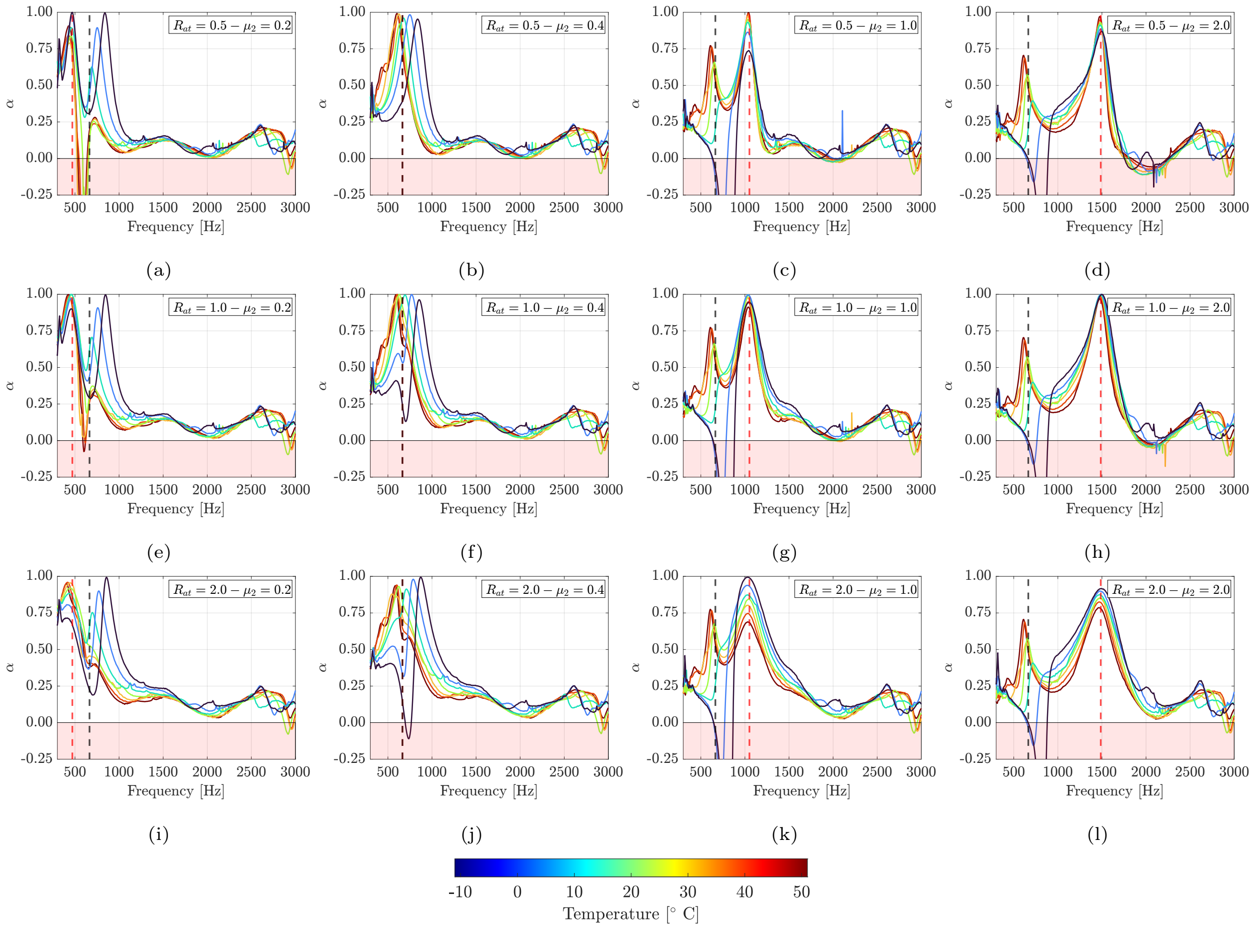

Figure 17: Results for the absorption coefficient with varying temperature and control parameters for cell A using constant Thiele-Small parameters: (a) $R_{at} = 0.5$ and $\mu_2 = 0.2$, (b) $R_{at} = 0.5$ and $\mu_2 = 0.4$, (c) $R_{at} = 0.5$ and $\mu_2 = 1.0$, (d) $R_{at} = 0.5$ and $\mu_2 = 2.0$, (e) $R_{at} = 1.0$ and $\mu_2 = 0.2$, (f) $R_{at} = 1.0$ and $\mu_2 = 0.4$, (g) $R_{at} = 1.0$ and $\mu_2 = 1.0$, (h) $R_{at} = 1.0$ and $\mu_2 = 2.0$, (i) $R_{at} = 2.0$ and $\mu_2 = 0.2$, (j) $R_{at} = 2.0$ and $\mu_2 = 0.4$, (k) $R_{at} = 2.0$ and $\mu_2 = 1.0$, and (l) $R_{at} = 2.0$ and $\mu_2 = 2.0$.

Conversely, a value of 0 indicates total reflection, with no absorption of the incident energy, and a negative value corresponds to the loss of acoustical passivity (reflected energy higher than incident one).

6.1. Control with fixed properties

Figure 17 shows the absorption coefficient results for cell A under Strategy #1. Each curve represents the absorption coefficient at a specific temperature, ranging from $-10°$C to $50°$C. Vertical dashed lines indicate the resonance frequency of the absorber (black) and the target frequencies (red). Regions where the absorption coefficient drops below zero are highlighted in red, indicating areas of negative absorption. In these regions, the EAs lose lose acoustical passivity and are subjected to possible instability when coupled with an enclosed cavity [6].

The EA employing a control law without adapting its properties to temperature variations exhibits multiple regions in which it loss passivity. For instance, it occurs for $R_{at} = 0.5$ and $\mu_2 = 0.2$ around 600 Hz, for all cases with $\mu_2 = 1.0$ and $\mu_2 = 2.0$ between 600 and 900 Hz, and for R_{at} and $\mu_2 = 2.0$ above 1700 Hz. These instabilities occur across the entire temperature range but are more pronounced at lower temperatures and lower frequencies.

Focusing on the tests with $R_{at} = 1.0$, Strategy #1 exhibits two regions where the absorption coefficient is close to one at low target frequencies ($\mu_2 = 0.2$). As the target frequency increases, the system begins to show instabilities around 700 Hz, with this behavior becoming more pronounced at higher target frequencies. Additionally, evaluating a line with constant R_{at}, e.g, Figs. 17i-l, strategy #1 appears to become non-passive as the target stiffness increases.

6.2. Control with varying Thiele-Small parameters based on experimental values

In Strategy #2, the measured Thiele–Small parameters for cell A are incorporated into the control law. Figure 18 shows the EA absorption coefficient for temperatures from $-10\,^\circ$C to $50\,^\circ$C. Compared with Strategy #1, which assumes constant parameters (Fig. 17), Strategy #2 yields markedly improved passivity around the target frequency. Instabilities are observed primarily at $-10\,^\circ$C when targeting frequencies at or below the absorber's resonance, i.e., $\mu_2 \leq 1.0$. In all scenarios, the EA exhibits non-passive regions at high frequencies, likely attributable to the phase lag introduced by control-loop delay, as demonstrated by De Bono et al. [6], and lack of validity for the 1DOF model implemented in the control law. This type of non-passivity appears insensitive to updating the Thiele-Small parameters with temperature. Nevertheless, the observed improvement in passivity near resonance underscores the value of temperature-dependent parameter updates.

6.3. Control with varying properties from the viscoelastic model

Given that experimentally testing each EA using a thermal chamber is neither practical nor cost-effective, and considering that correcting the Thiele-Small parameters can improve the operational passivity of these devices, Strategy #3 evaluates the feasibility of obtaining these parameters from the viscoelastic model and subsequently using them to update the control law.

Figure 19 presents the absorption coefficient results for cell D. Notably, the absorber remains stable across the entire frequency and temperature range, consistent with the results obtained for cell A under Strategy #2 and in contrast to the behavior observed under Strategy #1. Therefore, the viscoelastic model can serve as a reliable source of information for the control of the EAs.

7. CONCLUSIONS

This study investigates the impact of temperature variations on the mechanical properties of loudspeaker materials used in EAs. The results demonstrate that the system's natural frequency exhibits a non-linear

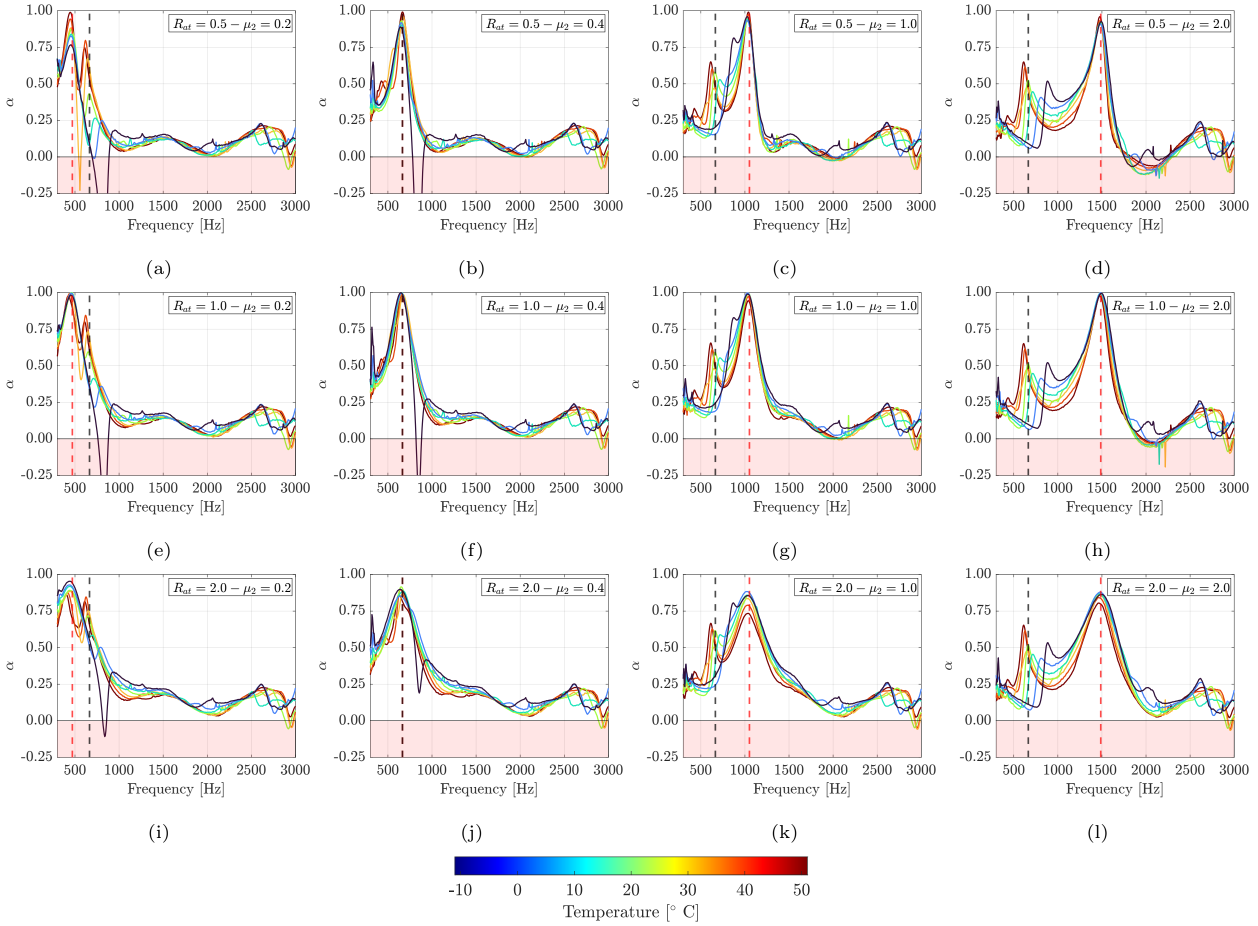

Figure 18: Results for the absorption coefficient with varying temperature and control parameters for cell A using variable Thiele-Small parameters: (a) $R_{at} = 0.5$ and $\mu_2 = 0.2$, (b) $R_{at} = 0.5$ and $\mu_2 = 0.4$, (c) $R_{at} = 0.5$ and $\mu_2 = 1.0$, (d) $R_{at} = 0.5$ and $\mu_2 = 2.0$, (e) $R_{at} = 1.0$ and $\mu_2 = 0.2$, (f) $R_{at} = 1.0$ and $\mu_2 = 0.4$, (g) $R_{at} = 1.0$ and $\mu_2 = 1.0$, (h) $R_{at} = 1.0$ and $\mu_2 = 2.0$, (i) $R_{at} = 2.0$ and $\mu_2 = 0.2$, (j) $R_{at} = 2.0$ and $\mu_2 = 0.4$, (k) $R_{at} = 2.0$ and $\mu_2 = 1.0$, and (l) $R_{at} = 2.0$ and $\mu_2 = 2.0$.

relationship with temperature, showing small variations of up to 8.1% at higher temperatures (50°C) and significantly larger changes of up to 31.9% at lower temperatures (-10°C) compared to the reference value at 20°C.

By identifying the Thiele-Small parameters from experimental frequency response functions, it was observed that the equivalent mass of the loudspeaker remains constant across the studied temperature range. In contrast, the stiffness and resistance display non-linear trends, with a noticeable transition around 20°C. This non-linear behavior is consistent with the viscoelastic nature of the materials used in loudspeaker construction.

To identify such material behavior, this study proposes three viscoelastic models, namely the fractional Zener, generalized Maxwell, and the generalized fractional Maxwell, to characterize the temperature-

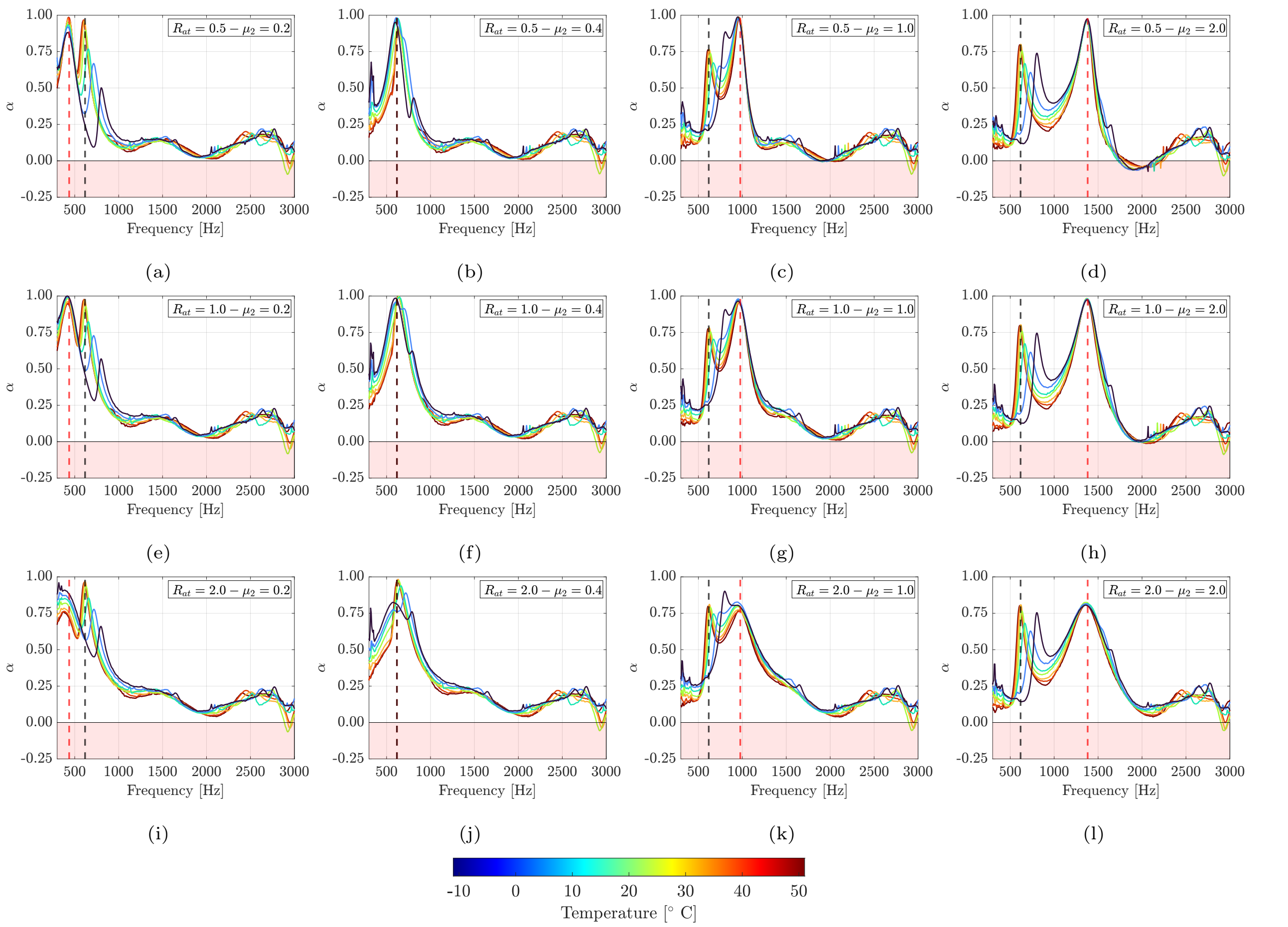

Figure 19: Results for the absorption coefficient with varying temperature and control parameters for cell D using variable Thiele-Small parameters based on the normalized viscoelastic model: (a) $R_{at} = 0.5$ and $\mu_2 = 0.2$, (b) $R_{at} = 0.5$ and $\mu_2 = 0.4$, (c) $R_{at} = 0.5$ and $\mu_2 = 1.0$, (d) $R_{at} = 0.5$ and $\mu_2 = 2.0$, (e) $R_{at} = 1.0$ and $\mu_2 = 0.2$, (f) $R_{at} = 1.0$ and $\mu_2 = 0.4$, (g) $R_{at} = 1.0$ and $\mu_2 = 1.0$, (h) $R_{at} = 1.0$ and $\mu_2 = 2.0$, (i) $R_{at} = 2.0$ and $\mu_2 = 0.2$, (j) $R_{at} = 2.0$ and $\mu_2 = 0.4$, (k) $R_{at} = 2.0$ and $\mu_2 = 1.0$, and (l) $R_{at} = 2.0$ and $\mu_2 = 2.0$.

frequency dependency of the materials. These models, fitted to experimental data using optimization algorithms, demonstrate varying levels of accuracy and computational efficiency. The Generalized Maxwell, particularly at higher orders, provides superior flexibility in capturing the complex material behavior compared to the Fractional Zener model, and a lower computational cost when compared to the general fractional Maxwell model.

A normalized viscoelastic model was developed using the average Thiele-Small parameters from three EAs, based on reference values at 20°C. This model was employed to estimate the parameters of an untested absorber, reducing the average error in the natural frequency compared to using constant properties based on the parameters measured at the reference temperature. Such a model enables the prediction of the properties of untested electroacoustic absorbers by integrating reference values with a generalized framework derived from tested materials.

Finally, the electroacoustic absorbers were evaluated in an active configuration to assess the effect of temperature on their passivity. In cases where the Thiele-Small parameters were not updated with temperature variations, the absorbers lost passivity and exhibited issues in multiple frequency regions, particularly near resonance. Correcting the parameters using experimentally measured data or properties obtained from the viscoelastic model improved passivity, with the latter approach proving to be a practical method for evaluating multiple absorbers with limited available information.

Future works could include analyzing the uncertainty associated with the Thiele-Small parameters to assess the convergence of the viscoelastic model as a function of the sample size used to construct the normalized model.

Another open research possibility is the evaluation of larger temperature ranges, specially for extreme operational temperatures, as turbo fan engines might experience both very low temperatures at cruise flight and high temperatures while operating in hot weather. The experimental apparatus used in this work could be expanded, including the characterization of the sensitivity of the microphones with temperature to evaluate potential impacts on the results and the evaluation of the capacity of the viscoelastic model to extrapolate in large temperature ranges.

ACKNOWLEDGMENTS

This work has been supported by the EUR EIPHI Project (contract ANR-17-EURE-0002) and Bourgogne-Franche-Comté Region. The authors would like to acknowledge Stani Cabrilet and the AMETISTE platform for the support during the experimental campaign.

REFERENCES

[1] K. Billon, M. Gillet, E. Salze, M. Volery, E. De Bono, M. Ouisse, H. Lissek, M. Collet, J. Mardjono, Smart acoustic lining for UHBR technologies engine: From the design of an electroacoustic metasurface to experimental characterization under flow, in: Active and Passive Smart Structures and Integrated Systems XVII, volume 12483, SPIE, 2023, pp. 390–396. doi:10.1117/12.2658519.

[2] H. F. Olson, E. G. May, Electronic Sound Absorber, The Journal of the Acoustical Society of America 25 (1953) 1130–1136. doi:10.1121/1.1907249.

[3] E. Rivet, S. Karkar, H. Lissek, Broadband Low-Frequency Electroacoustic Absorbers Through Hybrid Sensor-/Shunt-Based Impedance Control, IEEE Transactions on Control Systems Technology 25 (2017) 63–72. doi:10.1109/TCST.2016.2547981.

[4] K. Billon, E. D. Bono, M. Perez, E. Salze, G. Matten, M. Gillet, M. Ouisse, M. Volery, H. Lissek, J. Mardjono, M. Collet, In flow acoustic characterisation of a 2D active liner with local and non local strategies., Applied Acoustics 191 (2022) 108655. doi:10.1016/j.apacoust.2022.108655.

[5] E. De Bono, M. Collet, M. Ouisse, The Advection Boundary Law in absence of mean flow: Passivity, nonreciprocity and enhanced noise transmission attenuation, Journal of Sound and Vibration 590 (2024) 118603. doi:10.1016/j.jsv.2024.118603.

[6] E. De Bono, M. Collet, G. Matten, S. Karkar, H. Lissek, M. Ouisse, K. Billon, T. Laurence, M. Volery, Effect of time delay on the impedance control of a pressure-based, current-driven Electroacoustic Absorber, Journal of Sound and Vibration 537 (2022) 117201. doi:10.1016/j.jsv.2022.117201.

[7] M. Volery, X. Guo, H. Lissek, Robust direct acoustic impedance control using two microphones for mixed feedforward-feedback controller, Acta Acustica 7 (2023) 2. doi:10.1051/aacus/2022058.

[8] E. De Bono, M. Collet, K. Billon, E. Salze, H. Lissek, M. Volery, M. Ouisse, J. Marjono, Smart Acoustic Lining for UHBR Technologies Engine Part 2: Acoustic Treatment at the Intake of a Scaled Turbofan Nacelle, in: 30th AIAA/CEAS Aeroacoustics Conference (2024), Aeroacoustics Conferences, American Institute of Aeronautics and Astronautics, 2024. doi:10.2514/6.2024-3304.

[9] A. Novak, Modeling Viscoelastic Properties of Loudspeaker Suspensions Using Fractional Derivatives, Journal of the Audio Engineering Society 64 (2016) 35–44. doi:10.17743/jaes.2015.0091.

[10] P. Butaud, M. Ouisse, V. Placet, F. Renaud, T. Travaillot, A. Maynadier, G. Chevallier, F. Amiot, P. Delobelle, E. Foltête, C. Rogueda-Berriet, Identification of the viscoelastic properties of the tBA/PEGDMA polymer from multi-loading modes conducted over a wide frequency–temperature scale range, Polymer Testing 69 (2018) 250–258. doi:10.1016/j.polymertesting.2018.05.030.

[11] C. A. Henricksen, Heat-transfer mechanisms in loudspeakers: Analysis, measurement, and design, Journal of the Audio Engineering Society 35 (1987) 778–791.

[12] P. J. Chapman, Thermal simulation of loudspeakers, Journal of the Audio Engineering Society (1998). doi:https://aes2.org/publications/elibrary-page/?id=8513.

[13] M. Rousseau, J. Vanderkooy, Visco-elastic Aspects of Loudspeaker Drivers, in: 118th Convention of the Audio Engineering Society, AES, Barcelona, Spain, 2005. doi:https://aes2.org/publications/elibrary-page/?id=13240.

[14] B. Maillou, P. Lotton, A. Novak, L. Simon, Modelling nonlinear viscoelastic behaviours of loudspeaker suspensions-like structures, Journal of Sound and Vibration 416 (2018) 213–223. doi:10.1016/j.jsv.2017.11.046.

[15] N. Thiele, Loudspeakers in vented boxes: Part 1, Journal of the Audio Engineering Society 19 (1971) 382–392.

[16] R. H. Small, Vented-box loudspeaker systems-part 2: Large-signal analysis, Journal of the Audio Engineering Society 21 (1973) 438–444.

[17] ASTM International, Standard Test Method for Impedance and Absorption of Acoustical Materials Using a Tube, Two Microphones and a Digital Frequency Analysis System (E1050-24), 2024. Published May 1, 2024.

[18] R. Boulandet, H. Lissek, Toward broadband electroacoustic resonators through optimized feedback control strategies, Journal of Sound and Vibration 333 (2014) 4810–4825. doi:10.1016/j.jsv.2014.05.033.

[19] X. Guo, M. Volery, H. Lissek, PID-like active impedance control for electroacoustic resonators to design tunable single-degree-of-freedom sound absorbers, Journal of Sound and Vibration 525 (2022) 116784. doi:10.1016/j.jsv.2022.116784.

[20] E. De Bono, M. Morell, M. Collet, E. Gourdon, A. Ture Savadkoohi, M. Ouisse, C. H. Lamarque, Model-inversion control to enforce tunable Duffing-like acoustical response on an Electroacoustic resonator at low excitation levels, Journal of Sound and Vibration 570 (2024) 118070. doi:10.1016/j.jsv.2023.118070.

[21] K. Billon, E. De Bono, M. Perez, E. Salze, G. Matten, M. Gillet, M. Ouisse, M. Volery, H. Lissek, J. Mardjono, M. Collet, In flow acoustic characterisation of a 2d active liner with local and non local strategies., Applied Acoustics 191 (2022) 108655. doi:https://doi.org/10.1016/j.apacoust.2022.108655.

[22] B. Peeters, P. Guillaume, H. Van der Auweraer, B. Cauberghe, P. Verboven, J. Leuridan, Automotive and aerospace applications of the PolyMAX modal parameter estimation method, Proceedings of IMAC 22, the International Modal

Analysis Conference (2004).

[23] F. Renaud, J.-L. Dion, G. Chevallier, I. Tawfiq, R. Lemaire, A new identification method of viscoelastic behavior: Application to the generalized Maxwell model, Mechanical Systems and Signal Processing 25 (2011) 991–1010. doi:10.1016/j.ymssp.2010.09.002.

[24] M. L. Williams, R. F. Landel, J. D. Ferry, The temperature dependence of relaxation mechanisms in amorphous polymers and other glass-forming liquids, Journal of the American Chemical Society 77 (1955) 3701–3707. doi:10.1021/ja01619a008.

[25] R. Xiao, H. Sun, W. Chen, An equivalence between generalized Maxwell model and fractional Zener model, Mechanics of Materials 100 (2016) 148–153. doi:10.1016/j.mechmat.2016.06.016.

[26] R. L. Bagley, P. J. Torvik, On the fractional calculus model of viscoelastic behavior, Journal of Rheology 30 (1986) 133–155. doi:10.1122/1.549887.

[27] A. C. Galucio, J.-F. Deü, R. Ohayon, Finite element formulation of viscoelastic sandwich beams using fractional derivative operators, Computational Mechanics 33 (2004) 282–291. doi:10.1007/s00466-003-0529-x.

[28] M. F. P. Costa, C. Ribeiro, Generalized fractional Maxwell model: Parameter estimation of a viscoelastic material, in: NUMERICAL ANALYSIS AND APPLIED MATHEMATICS ICNAAM 2012: International Conference of Numerical Analysis and Applied Mathematics, Kos, Greece, 2012, pp. 790–793. doi:10.1063/1.4756256.

[29] D. Wang, D. Tan, L. Liu, Particle swarm optimization algorithm: An overview, Soft Computing 22 (2018) 387–408. doi:10.1007/s00500-016-2474-6.